Centro de Investigación en Materiales Avanzados, S.C.

Thesis

"A study of PLA-based polymer blends with lumbar fusion cage applications and its design evaluation through finite element analysis"

A thesis submitted in fulfilment of the requirements for the degree of

DOCTORADO EN CIENCIA DE MATERIALES

Presented by:

M.Ch.E. Luis Enrique Solorio Rodríguez

Directed by:

Dr. Alejandro Vega Rios

December 2019

Acknowledgements

I want to thank specially to my family: Silvia Rodríguez Méndez, Aidee Solorio, Victor Solorio and Ricardo Solorio. I will never pay all their support and I bless them eternally. Similarly, a profound feel of friendship and respect I want to state to my asesor and his family by all their attentions and advices professional and academically, whithout my asesor it was not be possible. Also, I thank to Dr. Alpizar by all the medical training, I will see you later friend!

I send special words to the following researchers. To Dr. Zaragoza: I remember very well the day that I met you at CIMAV, I could not forget that motivational words that you address to me during a internal presentation of the polymers group. I tried to follow all your advices, Thank you!

Dr. Velia Osuna: I thank you by the visionary opportunity and the faith deposited on me and all the chemical issues you taught me, I promised to be closer in the organic chemistry forever, Thank you!

Dr. Ivan Estrada: I will alwalys appreciate the respect and best wishes coming from you, specially in dark moments. Also, I tried to learn everything of polymer processing and other things. God bless you and thank you!

Dr. Alberto Diaz: I never imagined the potential of solid mechanics you showed me through all the way, I will miss you critics and teachings, Thank you very much!, and keep closer to San Juan Bosco.

Dr. Sergio Flores: Dear Dr. Sergio, during all my process in CIMAV, I saw your high skills and virtues as a scientific chief, I promise to be with you as you were with me.

Polymers group: you will be in my mind forever!; Erika López, Claudia Hernández, Mónica Mendoza, Barbara Farias, Jorge Olmedo, Jose Luis Espinosa, S. Conejo, Angélica Domínguez, Brandon, Miguel Aguayo, Marcos, Daniel Lardizabal, Luisa Camacho, Berenice Domínguez, Luis de la Torre, Ariane Paz, Emilio, Rodybeth Cruz, Miriam Carrasco, Lilian Tapia, Omar, Eider, the Sinaloa's crew, Tania. External friends:Meny Herrera, Meny Romero, Erik Romero, Mariana Huerta, Miraldelly Alvarez, Leo Robles, Alex Macías, César Perez. Dear Carlos Casas and Emmanuel: Thank you for all your friendship!, I hope to fill up the expectations…thank you…I love to all of you.

Reader (Whoever): Everything in this life is possible, I will see you in heaven!!

TABLE OF CONTENTS

LIST OF FIGURES

LIST OF TABLES

“Un estudio de mezclas poliméricas basados en PLA con aplicaciones a cajas de fusión lumbar y su evaluación de diseño a través del análisis de elementos finitos”

Luis Enrique Solorio–Rodríguez and Alejandro Vega–Rios *

Centro de Investigación en Materiales Avanzados, S.C., Miguel de Cervantes No. 120. C.P. 31136, Chihuahua, México;

luis.solorio@cimav.edu.mx ,*Autor correspondiente: alejandro.vega@cimav.edu.mx, Tel.: +52-01-614-439-4831

Resumen: El desarrollo de cajas de fusión intervertebrales involucra diversos factores entre los que destacan los materiales utilizados para la fabricación de estos dispositivos. Dentro de los mismos podemos encontrar metálicos y poliméricos, siendo los de tipo polímero quienes tienen una mayor demanda en aplicación e investigación en etapas académicas y piloto. Dentro de las desventajas que presentan las cajas de fusión intervertebrales fabricadas a partir de poli acetonas es que no pueden ser fabricadas debido que el material requiere condiciones de procesamiento muy alto, y esto requiere maquinaría especializada y costosa causando que los dispositivos sean caros. La biomecánica de trabajo demanda que el dispositivo tenga una buena resistencia a la compresión dado que las vértebras lumbares son quienes soportan el mayor peso en la columna vertebral. Otra desventaja de los materiales utilizados es que no presentan una biodegradación lo que implica la presencia permanente del dispositivo cuando es colocado en pacientes. En el presente trabajo se ha desarrollado una mezcla polimérica base PLA con las propiedades adecuadas para ser utilizadas con un potencial en cajas lumbares intervertebrales, teniendo como principal propiedad la biodegradación del material de una manera parcial. De la misma manera el material fue exitosamente impreso en 3d lo que puede extender la frontera de investigación para este material. De una forma paralela mediante el estudio de análisis de elementos finitos se obtuvieron los parámetros de diseño y se validaron con otros trabajos hechos en el área de simulación y se establecieron los parámetros a obtener para el material desarrollado. Las propiedades mecánicas se obtuvieron de manera experimental y los valores de módulo de Young y coeficiente de Poisson se alimentaron en el análisis de elementos finitos, y acompañados del diseño propuesto de una nueva caja intervertebral otorgaron los valores en desplazamiento y esfuerzos de von Mises de diseño. Después de efectuar la sustitución en uno de los discos intervertebrales por la caja intervertebral se obtuvieron los valores de desplazamiento y de esfuerzos von Mises. Los resultados mostraron excelentes propiedades mecánicas a la compresión compitiendo con el poli (éter éter) cetona y superándolo en la zona elástica. La simulación validó el diseño de la caja intervertebral con los reportes de otros autores y representa una opción de aplicación y sustitución como un material más económico y parcialmente biodegradable.

Palabras clave:PLA; análisis de elementos finitos, mezclas poliméricas, impresión 3d, caja intervertebral, fusión intervertebral

CHAPTER 1. GENERAL INTRODUCTION

1.1 Introduction

The present study aims to produce a polymeric material with proper mechanical properties to function as a lumbar fusion device. Rheological, thermal, and mechanical analysis were effectuated to analyze the physical and chemical structure of polymer and polymer/copolymer blends. Besides the analysis on polymer properties, a vertebral L1-L3 model was built and a finite element analysis was performed to evaluate the device functionality for biomechanical application.

Two sections comprise the whole methodology of this work. One describing the conditions on which the material was elaborated and its rheological and mechanical characterization. A second methodology explains the elaboration of a vertebral model and the results of the finite element analysis under flexion, torsion, and compression.

The results are presented in the following sequence: 1) a first finite element analysis on L1-L3 intact lumbar segment, 2) a study of polymer/copolymer blends analyzed and discussed, 3) a final comparison of the best-produced material through finite element analysis. Each chapter has a specific methodology, results, and conclusions. At the end of the whole work general conclusions are presented.

The following materials were elaborated and studied: poly (Lactide acid) PLA/(SMMA, poly (Lactide acid) (PLA)/copolymer (SMMA)/polyamide (PA 6).

The amorphous poly(lactide acid) (PLA) has lower Youn's modulus and elongation at break (%) than semi-crystalline PLA, which limits its diverse applications. To overcome this disadvantage, herein, we studied blends of amorphous PLA with a poly(styrene-*co*-methyl methacrylate) (SMMA) copolymer via melt mixing process. The blends produced also were fabricated in 3d printing filaments and then processed in additive manufacture. Poly(lactide acid)/poly(styrene-*co*-methyl methacrylate) (PLA/SMMA) blends were prepared varying compositions from 50, 75, 90 wt% of amorphous polymer. The polymer and copolymer demonstrated good compatibility through mechanical characterization. The $PLA_{80}SMMA_{20}$ has the highest Young's modulus than other blends. Also, this was verified by the behavior of the crossing point of storage (G') and loss modulus (G''). The complex viscosity of the $PLA_{90}SMMA_{10}$ blend, with higher PLA content, showed a lower complex viscosity than $PLA_{75}SMMA_{25}$ and $PLA_{50}SMMA_{50}$. On the other hand, the $PLA_{75}SMMA_{25}$ and $PLA_{90}SMMA_{10}$ presented a broad plateau in comparison with neat amorphous polymer and random copolymer. The glass transition temperature slightly increased in the blends, which supports the compatibility property. The material showed an appropriate facility to be printed in a final geometry. This blend is constituted from one biodegradable and a non-biodegradable polymer and copolymer respectively, and it represents a potential material for future medical devices.

The lumbar fusion cage design involves titanium and (PEEK) as materials. However, excessively elasticity modulus of Titanium surpasses the modulus of Cancellous bone and then subsidence can appear. PEEK is complicated of processing due to high thermal properties. This has occasioned that new polymer blends oriented to implant applications are under research. In this chapter, polymer blends of amorphous poly(lactide acid)

(PLA), poly(styrene-*co*-methyl methacrylate) (SMMA), and a polyamide 6 (PA6) were elaborated. The aim of this study was to evaluate the mechanical properties of a new material produced and to evaluate the performance under a desired shape through finite element analysis for the biomedical application as lumbar fusion cage. A model of L1-L3 levels was built and the number of elements analyzed were 2,364,541 in COMSOL Multiphysics® 5-3a. The compressive force, torsional moments and flexion moments were of 300 N and 7.75 and 5.85 N-m respectively. An excellent compressive strength resulted for the $SM_{20}PA_{10}PLA_{70}$ blend. The model was evaluated under two conditions: 1) without removing intervertebral discs and 2) by replacing the inferior IVD for a new design of fusion cage. Each condition faced three loading types: flexion and extension, lateral bending moments and compressive force. The results obtained in the finite element analysis were validated with pertinent literature. The von Mises stress were below from the stresses obtained in the experimental part, which ensure no failure for the device under given loads. This polymeric material represents a potential candidate to compete with more expensive polymers in similar biomedical applications.

1.2 Motivation and Objectives

About 160 000 thoracolumbar injuries per year are registered in the United States of America. From these, lumbar injuries are more often found in men approximately by one third more in population than women. The older people is, the risks of having a lumbar pathology increases. Similarly, accidents produce lumbar trauma pathologies. High-energy fall accidents (falls above 2 m of height) had a 39% of appearance followed by traffic accidents (58%) in an injury study. The highest spine level fractured was the lumbar with 28.5% of all spinal segments and being L1-L3 those levels more affected. [1,2] Based

on the statistics, a L1-L3 vertebral model was developed and analyzed through finite element analysis. The simulation adds important information as: 1) parameters of a polymeric material design intended for lumbar fusion cage used by other researchers, 2) A geometry approximation to natural components regarding biomechanical issues, 3) The behavior of materials under different shapes and its validation under application. Regarding materials properties, the structure and processing of the commercial materials used in lumbar fusion cages are constrained to specific conditions. High-performance polymers are dominating the market being expensive and difficult to process, what indicates new polymer blends are required. Polymer materials must be employed to replace metallic alloys and materials because of their softer mechanical properties closer to natural human body components. These materials must be affordable concerning cost and processability issues. From a mechanical point of view, the materials destined to be used in lumbar fusion cages should have: lower Young's modulus than cortical bone, because the excess of Young's modulus value can grant closer mechanical behavior to natural components present in the lumbar segment. In this study two polymer blends are developed and discussed as a new option for these kind of medical devices.

1.2.1 Hypothesis

The development of PLA-based polymer blends with other biomaterials produce adequate mechanical properties for lumbar fusion cage design and whose mechanical performance can be validated through finite element analysis.

1.2.2 General objective

To develop PLA-based polymeric blends with suitable properties for the application of the lumbar fusion cage through finite element analysis.

1.2.3 Specific objectives

To produce polymer blends PLA/poly(styrene-co-methyl methacrylate) (SMMA) and SMMA/PA6/PLA.

To establish the optimal processing conditions and the proper characterization techniques.

To develop the 3D printing filament of the materials and to print them through 3d printing process.

To simulate the polymer blends behavior under application via finite element analysis (FEA).

CHAPTER 2. BACKGROUND AND LITERATURE REVIEW

2.1 Spine morphology

The vertebral column contains essential functions and morphological components, where the brain and the spinal cord comprise the central nervous system. The spinal cord has the aim of leading information across the body. This spinal cord is protected from injuries by vertebrae. The entire spinal cord is divided into 31 sections, which are labeled C (cervical), T(thorax), L(lumbar), and S(sacrum). A number is associated with each letter to locate the segment and number of level. A pair of dorsal root ganglia is linked to each segment posteriorly containing the sensory neurons. In the anterior plane, a ventral root holds the axons of somatic motor neurons. Also, there are 26 vertebrae and 31 pairs of nerves. The vertebrae provide the support necessary to keep stability. Each vertebra is connected to another adjacent through the articular facets and intervertebral discs. Along with the extension of the vertebral column, there are four curves: cervical, thoracic, lumbar, and sacral curves. The main bony components of a vertebra are pedicles, vertebral arch, vertebral body, an inferior and superior process, transverse process, vertebral foramen, lamina, and spinous process. Between each intervertebral level, there is a cartilaginous articulation named symphysis. This kind of articulation belongs to amphiarthrosis; it does mean an articulation with little motion and constitutes the intervertebral disc. It has two main functions: 1) to separate individual vertebrae and 2) to transmit the load from one vertebra to another. The annulus fibrosus and nucleus pulposus constitute the intervertebral disc. There are four movements allowed for the vertebral column: flexion, extension, bending, and torsion.[3] Briefly, the pathologies that

can suffer the spine, such as lumbar spinal stenosis, degenerative disc disease, lumbar fractures, degenerative kyphosis, and degenerative spondylolisthesis are due to various factors such as human activities, accidents, and age. Next, a few pathologies are described:

Lumbar spinal stenosis. Lumbar spinal stenosis is defined pain in the lower extremities of the back or buttock manifesting with or without pain.[4–6] Furthermore, stenosis can sometimes be improved through a surgical procedure using gold or inter-spinous spacers to limit the movement of the segment in extension, which releases compression of the canal.[6,7,8] When severe stenosis is diagnosed, the laminae are removed, and a partial resection of the facet is performed, with the risk of postoperative complications.[9]

Degenerative disc disease. Degenerative disc disease is caused by negative pressure within the disc havinga mechanical deterioration observed by nuclear magnetic resonance. Eventually, the disc can move radially across the intervertebral space causing bulging or herniation depending on the circumference covered.[10] Protrusion and extrusion of the disc herniation signify two scenarios: 1) if the base disc is more significant than another measurement in the same plane of herniation, it is called protrusion; 2) when any other measurement of the herniation is higher than its measurement in the base, it does mean extrusion.[11] On the other hand, the main procedures used in the cure of degenerative lumbar disc disease are total disc replacement (TDR), anterior and posterior lumbar interbody fusion (APLIF), posterior lumbar interbody fusion (PLIF), posterolateral interbody fusion (PLF), anterior lumbar interbody fusion (ALIF).[12]

Lumbar fractures. These occur due to exaggerated movements of vertebrae, classified as axial deformation, torsion or axial rotation, segmental translation, combined mechanisms.[2,13] Lencean (2003) reported classification of spinal injuries based on the essential traumatic spinal mechanisms, and he reported 314 cases, covering cervical, thoracic, lumbar, and lumbosacral vertebrae. The fractures come when exaggerated motions of vertebrae occur. These motions can be classified as axial deformation, torsion or axial rotation, segmental translation, combined mechanisms.[2,13] Focused on daily activities, Leucht et al. reported that the spinal cord is injured 10-30% when traumatic fractures happen. In addition, the most common accident was high-energy fall, followed by traffic accidents. The first involves injuries over the global spine, whereas the second covers cervical and thoracolumbar segments.[1] Similarly, Pedram et al. reported the same order of vertebral fractures: falls and road traffic crashes, where the most affected segment was lumbar.[14]

2.2 Fusion cages

The aim of the fusion cage is to fusion biomechanically, preserving the disc height, and protecting nerve roots when a pathology must be solved. Since the first appearing and application of these devices by Capener (1932) for the treatment of spondylolisthesis in a group of 32 patients,[15] and Cloward (1940),[16] other devices which accompany these devices are metallic screw and rods, which are used to stabilize the damaged segments. However, the devices show an increase in stiffness concerning natural biomechanics.[17] Attempts to approximate to the prediction from intact lumbar and instrumented segments

have been done. Lee et al. simulated the behavior of titanium versus porous titanium fusion cages.[18] Today there are many designs of fusion cages, but Brantigan cages are the most used composed primarily of titanium and PEEK. There are diverse designs among lumbar fusion cage patents, for example, a lumbar fusion device with truss spaces to facilitate bone surface was patented; the materials for this device include titanium alloy, stainless steel, and PEEK.[19]

Escrivano et al. reported excellent outcomes when using these Brantigan cages with a 100 fusion rate percent in 7 of 10 patients being L4-L5 and L5-S1 the primary levels among the pathologies studied.[20] However, subsidence appeared at the time, showing the rigidity of the material, more often when using titanium.[21] The term subsidence refers to the physical volume indentation into the vertebra, once implanted. To overcome subsidence, new materials are sought, and new patents have appeared. Unfortunately, many patents define just embodiments or proposals and do not mention the maximum mechanical properties of the materials under the patent design. Generally, most of the cages involve just the design; for example, another invention describes an expandable cage to extend the device once implanted. This allows a minimum invasive surgical technique and provides adequate dimensions to give lumbar support.[22] Another design considered the retaining of fluids or the bone graft and the fixation of the cage towards the external boundaries.[23] In addition, there is an invention of cage design with the purpose to facilitate the distraction of the vertebrae involved, through modification by rotating the tip of the cage, allowing proper distraction.[24] Similarly, there is also another design with internal blades (the fixation system), whose blades extent once placed, these types of designs are also suggested in titanium and PEEK.[25] In addition, inflatable devices

are being proposed, like the *in situ* fusion cage put in a cannula, to complete the height of a degenerated disc. This way, increasing the volume of a balloon injecting material viscous fluids, which surface can be of various materials (PMMA, PE, PC, and others) including fibers registered commercially.[26] As we stated, most of the patents are currently interested more in design than materials issue.

2.2.1 Commercial cage materials

Lumbar fusion cages are commercially available in PEEK and titanium. In the next paragraphs, we describe a few physical and chemical properties of both materials. Similarly, a brief revision of hydroxyapatite (HA)/PLA composites is also included.

2.2.1.1 Poly(ether-ether-ketone) (PEEK)

PEEK is a semicrystalline polymer very popular for cage manufacturing with high thermal and mechanical properties. In addition, the main producers are Invibio Thorton-Cleveleys, Victrex, Solvay, Evonik.[27] The mechanical properties, like Young's modulus, is 2.699 GPa and a density from 1230 to 1650 Kg/m^3 reporting a value of μ=0.36 for the Poisson coefficient.[28] One fundamental property is the elongation of PEEK, which is reported in an elongation range also considering the plasticized zone.[29-30] So, it is imperative to notice that in the elastic zone this material attains 2-4% approximately and this value should be set for designing purposes because a material surpassing the elastic limit point or yield point will not return to its initial shape.

PEEK has an orthorhombic structure with two molecules forming the mainframe through the edges and therefore passing in the vertex of each unit cell. The width and length of the cell are 0.586 nm and 1 nm respectively.[31]

The Young's modulus of PEEK is between the cortical and the cancellous Young's modulus (3.5 GPa), causing also that many studies look to reinforce when harder bone applications are sought. Similarly the use of PEEK as matrix is commonly addressed for increasing bioactivity interest.

Nanocomposite materials found in the literature are tricalcium phosphate, titanium, hydroxyapatite, and carbon fibers. The main effect that these fillers regarding the PEEK matrix are to increase from 1.36 up to 7.5 times Young's modulus.[32] Bioactivity is essential when evaluating, but for mechanical stress analysis the only thing to keep in mind is the reinforcing character and that if the polymer is not biodegradable, the mechanical properties remain.

The processing at high temperatures and annealing or quenching is a common process found when processing PEEK. Only very selective machinery can attain this processing temperatures (360 °C and more). Crack growing, impact and fatigue material behavior are factors to be considered when implant cages are designing.The cyclic life decreases when the micro and physical small crack regions are present in PEEK matrix.[33] Few research works have published with results of high wear behavior of PEEK and PEEK reinforced in comparison with ultra-high molecular weight polyethylene (UHMWPE), supporting the idea to keep looking for new materials besides PEEK to avoid this behavior.[34]

2.2.1.2 Titanium

Porous titanium materials providing low Young's modulus are to give the optimum mechanical properties. Some problems as wear, fretting,[35] and subsidence also can be presented. PEEK presents more difficulties when attained to the bone endplates, it is attributed may be to the inert boundaries. The titanium cages continue today in the lumbar application because they have a better surface modification characteristic than PEEK.[36] The subsidence was observed little higher, but no with a big difference in bio-glass cages than in titanium cages, and the same for the Visual analog scale (VAS) and Oswestry disability index (ODI) outcomes, what means titanium can give results resembled ceramic materials. Typical titanium implant cages are composed mainly of vanadium and aluminum, but there are traces of Si, Fe, Ni, Cr, and others (Ti 6Al 4V).[37] Titanium has weak shear strength at long-term using; [38] besides, notches can produce the fatigue quickly, which can be presented in cage teeth (a tooth acting as a notch). Also, the peaks can produce higher stresses by the reduced area. Furthermore, different alloys are developed seeking better non-inflammatory reactions and giving lower Young's modulus to keep up better properties.[39] Thus, ionic metals on titanium through diverse processing methods, give better conduction for bone formation. However, at the same time, it increases the hardness of the material,[40] what does not fit well with the hardness of cancellous bone.[41] This last ten times lower (Hardness Vickers) approximately than titanium,[42] what can also be a cause of subsidence initiating phenomenon.

The crystallinity is rarely found in literature when talking about biomaterials and comparing them, is a crucial issue when analyzing biomaterials. Titanium and its alloys present high crystallinity due to the titanium metal atoms order.[43-44] The chemical

structure of these materials is different since one is a metallic bond, whereas the other has covalent bonds. Titanium otherwise presents a defined structure, the phases found are the α phase having a hexagonal close-packed structure; and by the other hand and the (α + β) phase, what is an intermediate phase and its crystalline structure belongs to a body-centered cubic.[45] At room temperatures, the titanium alloys could have both phases: the alpha and the beta. The first one is known as unalloyed titanium, and it can be stabilized with aluminum, for example. The beta phase is at high temperatures, but it appears at room temperatures by adding elements like vanadium, molybdenum, chromium, or iron. The tensile strength, yield strength, and elongation at break (%) are of about 860 MPa, 780 MPa, and 10 % respectively.[38] In addition, density, Poisson coefficient, and Young's modulus are essential to simulate the material behavior through finite element analysis. It is worth to mention that titanium is also used in rib-base devices as the anchor to alleviate spine deformity. [46] It is reported that the selection of cages must be not just a dimensionally manufacturers affair, but a decision grounded on physiological patient data.[47] Today the most used materials are PEEK and Titanium,[21] which are processed to be porous, therefore facilitating the osteoconductivity in the application. Unfortunately, both materials present higher Young's modulus still in comparison to the natural bony components. Also, the density as a function of Young's modulus must be considered.[48] Authors in the simulating issue report different values of E for the cancellous bone, ranging from MPa to about 4 GPa.[49-50] Mainly there is a lack of knowledge of the stresses presented in the lumbar bone components due to the fusion devices, what comes from the core of the material's structure and which topic is never explained in other reviews.

2.3 Additive Manufacturing

The additive manufacturing (AM) is going to be more present when specific products are desired. The projection for 2030 estimates that more than 50% of the overall industrial AM capacity will be in-house production capacity and manufacturing. Additionally, the spare parts will be divided into two systems: less critical parts will be produced locally via additive manufacturing, whereas critical parts will be made at specialist hubs with specific qualification/quality control skills, primarily using conventional manufacturing techniques.[51] Among the AM processes available high-temperature laser sintering (HT-LS) is the newest via on which PEEK implants can be processed. This additive manufacturing technique does not require the robust machinery used to get high production volumes. The powder bed fusion is attacked with a CO_2 laser.[52] It is important also to mention that today there are just a few products with medical-grade used in the additive manufacturing, OXPEKK® supplied by Oxford Performance Materials and e PEEK OPTIMA® LT1 grade, from Invibio Biomaterial Solution. This last which has been traditionally processed in extrusion and molding. For titanium, also the AM has been developed, and the Selective Laser Melting Technique (SLMT) is being used. A research work did report material from Ti_6Al_4V-PEEK, designed to evaluate a possible morphology when using (SLMT) and the wear performance. The results showed proper morphology for cell structure adhesion and a better wear behavior with improvement up to 40% in the lower mass loss when compared to casted/forged materials used in implants.[53] Regarding 3d printing technology for metallic devices among AM technologies, there is limited information. Most of the reports are addressed to electron beam melting (EBM) and selective laser melting (SLM).[54]

2.4 Design of lumbar fusion cages

The lumbar cage design is crucial when implant-making is being developed; in this study, a patent revision was done before the experimental procedure to know the main features and shapes used in lumbar fusion cages. The lens website (http://www.lens.org) was used to search for patents. Lens collects published patent applications from 115 million patent documents. Accessing to the Lens website, an advanced search using keywords in patent titles and summaries was carried out. Next search terminology was used: intervertebral fusion cage, lumbar interbody fusion, lumbar spine simulation, lumbar fusion cage finite element, lumbar articular facets, PEEK, and titanium lumbar fusion cage.

CHAPTER 3. FINITE ELEMENT ANALYSIS INTACT MODEL

3.1 Introduction

3.2 Modeling and simulation

A model constituted of three vertebrae, two intervertebral discs, two pairs of facet capsules linked to pedicles, and the anterior ligament was built. COMSOL Multiphysics® as CAD software was used. The appropriate morphology was based on the literature.[55] 2,065,077 tetrahedral, 282,496 triangular, 16,389 edges and 579 vertex elements were analyzed. The parameters used for each domain and the associated material are listed in Table 3.1.

A similar research reported a non-linear lumbar model consisting of five vertebrae, intervertebral discs, and spinal ligaments. The aim of that study was focused on the lateral bending behavior in the lumbar segment.[56] Another group reported the facet tropism in the lumbar spine by using a model comprised of four vertebrae, three intervertebral discs, and associated ligaments.[57]

Similarly, an L3-S1 finite element model was constructed by another research group, which topic of studying was the anatomic facet replacement system (AFRS) when facet joints are replaced.[58] This last work analyzed 31054 elements and 38,664 nodes.

Table 3.1. Model parameters

Domain	Type of material	Poisson's coefficient	Young's modulus (MPa)	Author
Domain 1 Cortical bone	Linear	0.3	12000	[59]
Domain 1-A Cancellous bone	Linear	0.25	200	[58]
Domain 1 articular inferior facet	Linear	0.3	12000	[59]
Domain 2 Intervertebral Disc	Mooney-Rivlin Hyperelastic	C_{10}=0.12 (MPa)	C_{01}=0.09 (MPa)	[60]
Domain 3 cortical bone	Linear	0.3	12000	[59]
Domain 3 cancellous bone	Linear	0.25	200	[58]
Domain 3 articular superior facet	Linear	0.3	12000	[59]
Domain 4 facet capsules	Linear	0.4	11	[58]
Domain 6 anterior ligament	Linear	0.3	11	[58]

3.2.1 Applied load

Values from 250-1000 N were found in an experimental work where load in children's bag was evaluated.[61] Another work reported an appropriate posture that can diminish the loads produced when lifting different weights, being the spine load used of 400 N.[62] Also, the flexion-extension values in the anterior-posterior shear forces were analyzed by using a force of 500 N[63] in degenerative disc measurements. In the compressive tests some authors used 600 N[64] and others loads of 200 N[65] and 1750 N[66] when considering muscle activity but these last using a whole spine morphology. Lumbar

spine loads in a dummy were simulated, registering compression and shear loads under a backpack charging of 2500 and 800 N. [67]

The first simulation covered the lumbar model with intact intervertebral discs. The second remained with the superior disc, but the inferior was removed and substituted by the device. Both simulations included: 1) a compressive force axially of 300 N, 2) flexion and lateral moments of 5.85 Nm, and lastly 3) torsional moments of 5.85 and 7.75 Nm. The compressive forces acted over z-axis, while flexion and torsional moments acted on y and y and x-axes (Figure 3-1). The value for each lateral moment applied was of 5.85

Nm on the model. The lateral bending was applied to the x axis direction, and the flexion moment was applied to the y axis direction.

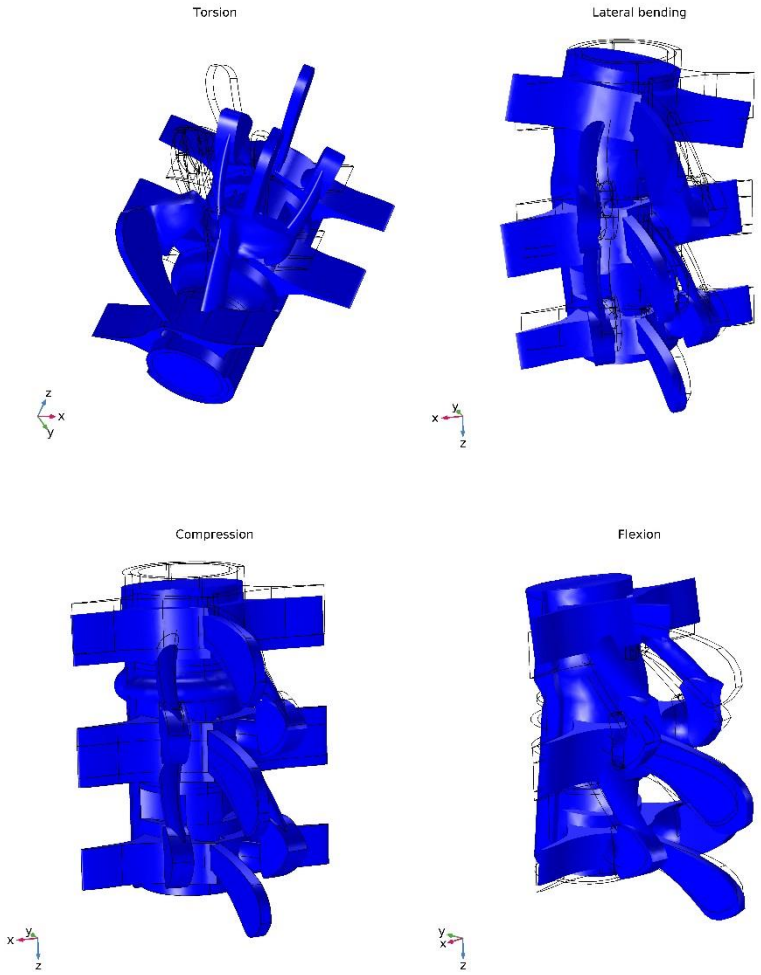

Figure 3-1. Motion of the L1-L3 model. Upper left: Torsion, Upper right: lateral bending, bottom left: compression and bottom right: flexion

3.3 Results and discussion

3.3.1 Model with natural discs

3.3.1.1 Flexion moment on intact model

Figure 3-2 shows the von Mises stress and total displacements for a flexion moment. Under a moment of 5.85 Nm the superior and inferior intervertebral discs (IVD's) had 0.3 and 1.14 MPa. The highest von Mises stresses were in the pedicles cause the change of section in geometry. The deformation item was scaled 7 times to show the deformation on the model. Similarly, Bouzakis et al. evaluated the von Mises stress of cortical and cancellous bone, reporting values in the range of 0.43-0.88 and 0.57-2.2 MPa for cancellous bone and cortical bone, respectively.[68] They also reported, relative displacements of cortical and cancellous bone of vertebrae with a maximum value of 2 mm.[68] Another work evaluated three different cages and its positions on the intervertebral disc space. The cortical bones when placing two cages laterally produced von Mises stresses of 14.382 and 7.138 MPa for flexion and extension, respectively. These von Mises stresses were 4.6 times higher when placing the cage anteriorly than when using

two lateral cages. The superior IVD had a maximum displacement value of 0.86 mm, while the displacement of the inferior IVD was of 1.03 mm.

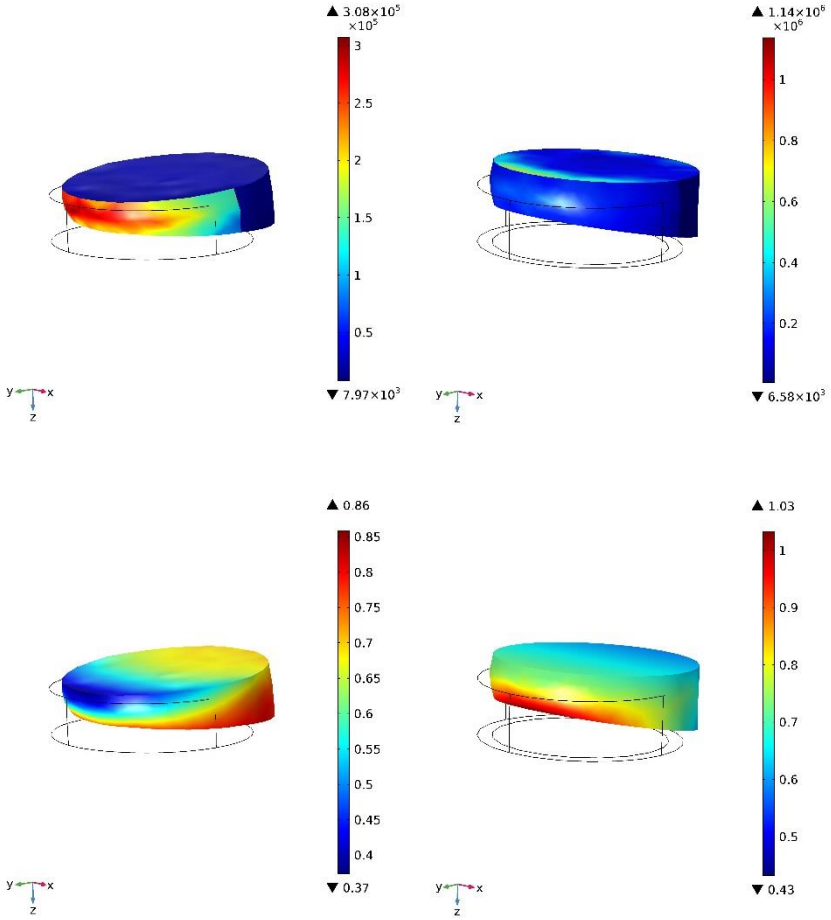

Figure 3-2. Upper: Flexion von Mises stresses (Pa) of superior and inferior IVD's. Bottom: displacements of both discs.

The displacements of natural discs were in the range of 0.5-0.7 mm. In another work, a robust table containing the displacement of lumbar intervertebral discs was reported.[69] Marini et al.[70] found that under biomechanical compressive tests on human lumbar discs,

relative displacements of 1 mm were registered. There is a wide range among displacements, but almost all fit well with our results.

3.3.1.2 Compression

In the intact model, the first vertebra of L1-L2 and the superior IVD had the highest displacement of about 0.96 mm under a compressive force of 300 N (Figure 3-5). These displacements are in the range of other reports. [17] [18] [70] [71] Also, the displacements of facet joints were in the range of 0.3-0.48 mm. The L2-L3 facet joints had lower displacements than the superior facet joints. These displacements were closer to similar displacements of facet joints evaluated in another report, which evaluated facet joint displacements through dynamic stereo radiography (DSX) imaging. The displacements were evaluated in ten participants and L2-S1 levels. They lifted three weights, starting from a trunk-flexed

position to an upright position. [72] The inferior IVD presented maximum displacements of about 0.4 mm (Figure 3-3).

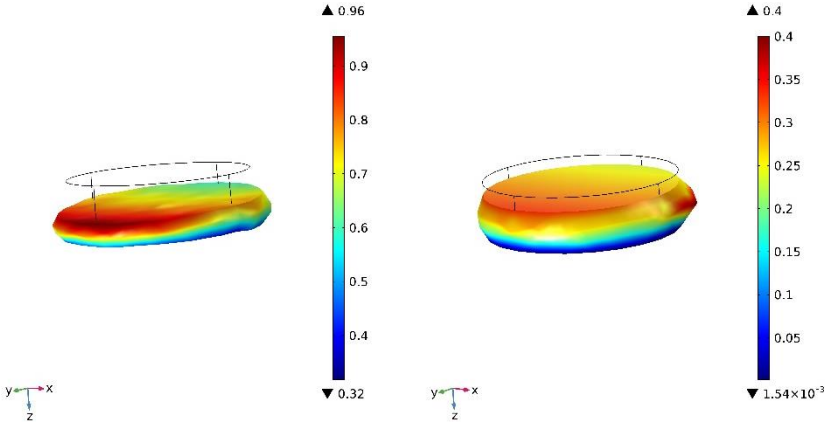

Figure 3-3. Displacements (mm) under compression. Superior IVD (left) and inferior IVD (right) on axial direction

The von Mises stress was higher in the pedicles due to the stress concentrations. These values had a maximum value of 6.87 MPa. The vertebrae von Mises had values in the range of 0.41-1.9 for the cortical bone of L1-L3 and its transverse apophysis. These values are closer to those reported in another work which reported von Mises results under compressive force. The values were from 0.57 to 2.2 MPa. [68]

The Maximum von Mises values for the superior IVD were of 0.42 MPa, whereas the inferior presented a higher value with 0.89 MPa (Figure 3-4).

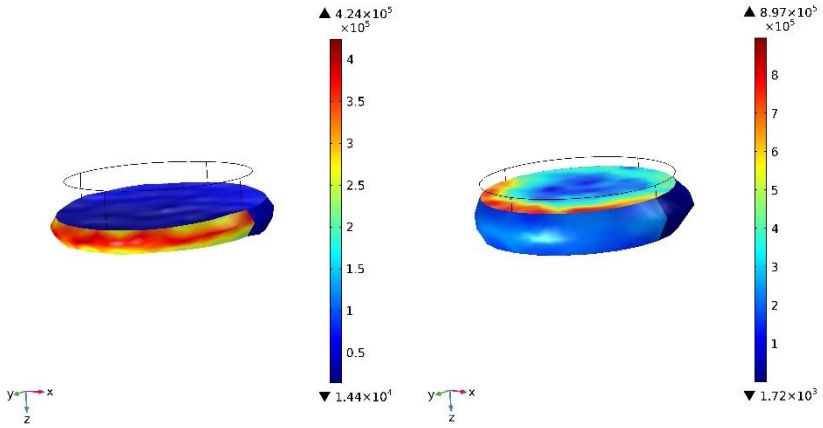

Figure 3-4. von Mises stresses (Pa) under compression. left: superior IVD, right: inferior IVD

3.3.1.3 Torsional moments

A torsional moment of 7.75 Nm was applied to the intact L1-L3 model. The maximum displacements were present at the L3 level. The inferior IVD had 2.09 mm of maximum displacement whereas de superior IVD had 1.8 mm. The maximum displacements were observed in posterior plane and bottom for the superior IVD. The inferior IVD presented more displacement along the cortical bone of the IVD . The von Mises stresses also were higher in the inferior IVD with a value of 4.26 MPa. The superior presented 0.85 MPa as maximum value (Figure 3-5).

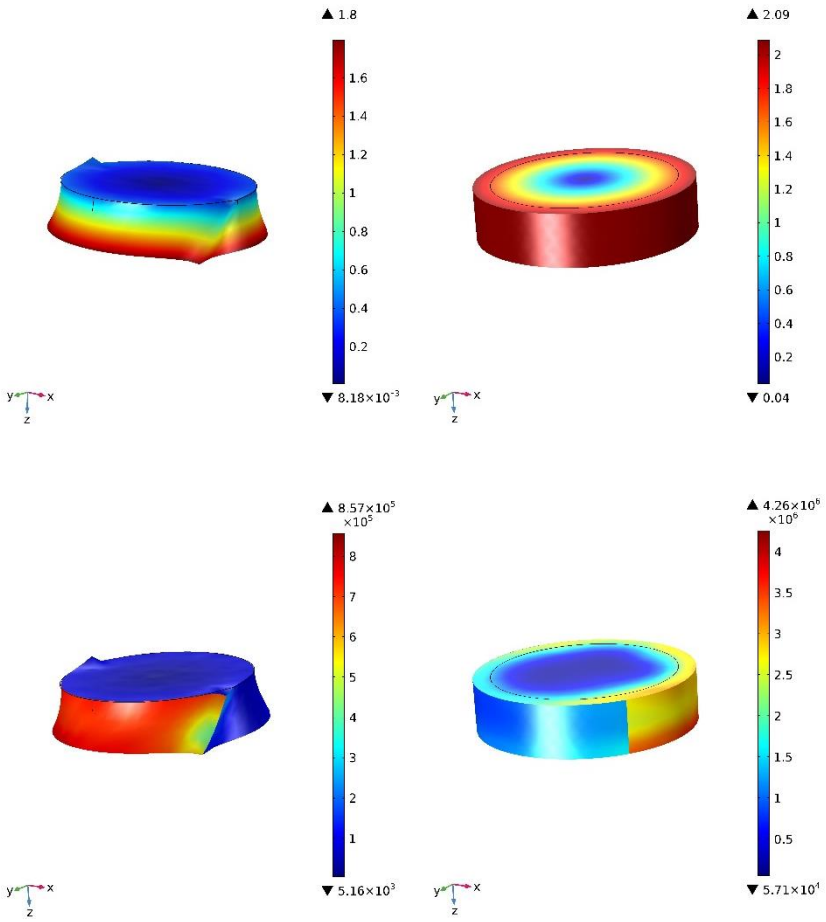

Figure 3-5. Torsional displacements (mm) and von Mises stresses (Pa). upper left: superior IVD displacement, bottom left: inferior IVD displacement. Upper right: von Mises of superior IVD, bottom right: von Mises stresses of inferior IVD.

3.3.1.4 Lateral moments

In this work, the von Mises stress in the natural disc was about 1.65 MPa for lateral moments (Figure 3-6). Asgharzadeh et al. reported a closer value to our results (3 MPa) under a bending moment of 5 Nm.[71] Also, lateral bending moments of 5.85 Nm were applied in the work of Lee at al. (2016).[18] von Mises stress of about 300 MPa was obtained for vertebrae when using a single titanium porous cage centered in the intervertebral disc space. In Figure 3-6 displacements of the model are shown. The displacements due to lateral bending moments were higher than flexion. The von Mises stresses in the superior

and inferior IVD were of 0.63 and 1.65 MPa. The bending moment over -X produced displacements from 1.3-1.7 mm in the superior IVD, while for the superior disc the values attained 2.14 mm in the inferior IVD. Higher displacements were found in the bending moment over +X.

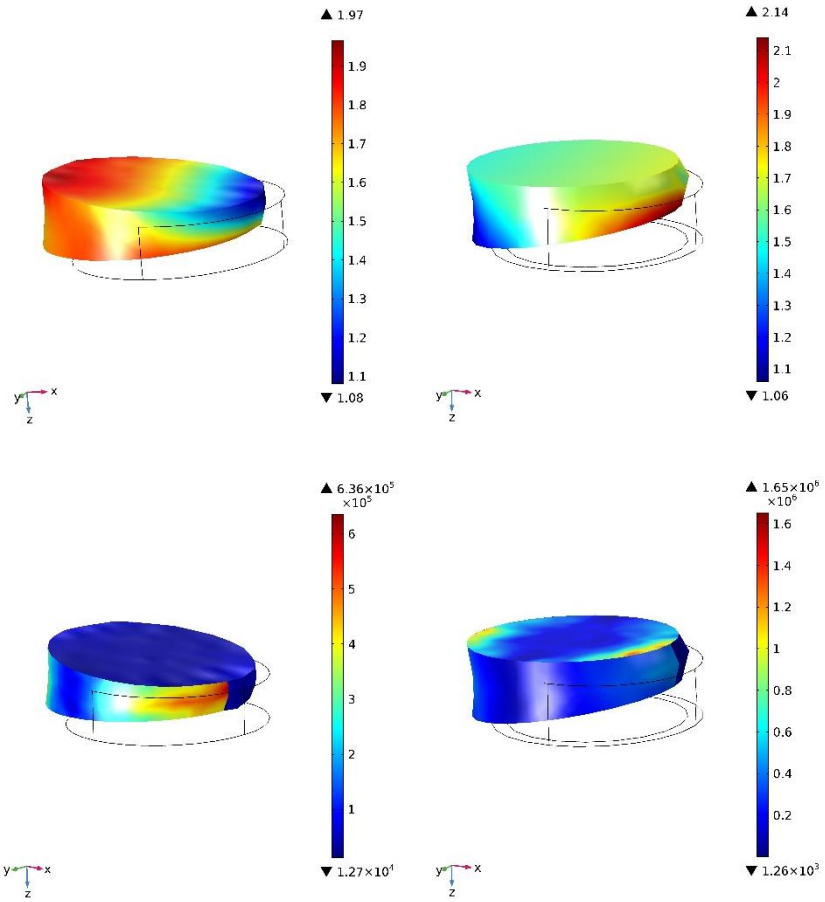

Figure 3-6. Lateral displacements (mm) and von Mises stresses (Pa). upper left: superior IVD displacement, bottom left: inferior IVD displacement. Upper right: von Mises of superior IVD, bottom right: von Mises stresses of inferior IVD.

3.4 Conclusions

An L1-L3 model was built, which was evaluated without removing intervertebral discs and three loading types were applied: flexion and extension, lateral bending moments, and compressive force. The results obtained in the finite element analysis were validated with literature. The geometry of the model was validated with *in-vitro*/*in-vivo* research works, and maximum von Mises stress and displacements of the L1-L3 intact lumbar segment were obtained. Table 2 compares the present results of the intact finite element analysis with other authors.

Table 3.2. von Mises stresses compared with other studies

Author	von Mises stresses in intervertebral discs (Mpa)	Motion
Yung-Heng Lee at al. (2016)	2	Flexion (6 N.m) 2 fusion cages in the extremes of the cancellous bone still without fusion (L3-L4)
Kim et al, The Spine Journal, (13)(2013) 1301-1308	0.3	Flexion (7.5 N.m)
Tsai et al, Computers in Biology and Medicine 76 (2016)14-23	<2	Flexion (7 N.m)
Fantigrossi et al, Medical Engineering and Physics, 29 (2007)101-109	0.2	Compression (250 N)
Present study	1.14 (flexion) 0.89 (compressión) 1.65 (Lateral bending) 4.26 (Torsion)	Compression (300 N), flexion and lateral bending (5.85 N.m), Torsional (7.5 N.m)

CHAPTER 4. POLYMER BLEND POLY(STYRENE-*CO*-METHYL METHACRYLATE)/POLYLACTIDE

4.1 Introduction

Poly(styrene-*co*-methyl methacrylate) (SMMA) is a random copolymer with advantages over neat polystyrene (PS) and polymethyl methacrylate (PMMA). It has a M_w=150 000 g/mol Its synthesis comes from radical polymerization of styrene and methyl methacrylate monomers and a polydispersity index in the range of 1.9-2.3. its density ρ=1.04-1.13 g/cm^3 with colorless and odorless properties. A few manufacturers are: Ineos Styrolution, Shin-A under NAS, Zylar and Claradex trade marks. The features are sparkling clarity, low density, and ease of processing with applications in medical devices, cosmetics jars, and lids, reusable drinkware, toys, office accessories, mainly, according to Ineos Styrolution manufacturer. The styrene and methyl methacrylate content on SMMA is ranged from 70 to 90 wt % and 10 to 30 wt % , respectively, according to the patent number EP3068834 B1.[73]

Additionally, SMMA has been used as the compatibilizing agent (2-10 wt %) in polymer blends of polystyrene copolymers and PLA (10-30 wt%), high-impact polystyrene (HIPS, > 50 wt %) or PS (~ 50 wt %) according to the patent number US 10,072,144 B2. Also, other examples of polystyrene copolymers are styrene-acrylonitrile copolymer, acrylonitrile-butadiene-styrene copolymer, styrene-butadiene copolymer, styrene-maleimide copolymer, and styrene-*alpha*-methylstyrene copolymer. Likewise, the polymer blends of PS, PMMA, or PS/PMMA have several reports concerning miscibility

and/or compatibility.[74,75] Contrarily to these last reports, other authors supported immiscibility of PS/PMMA blends.[76,77]

On the other hand, the different alternatives that exist to mix the polylactide (PLA) with other (co)polymers, especially with those from fossil fuels, can generate polymer blends with specific characteristics or properties for a given application.[78] Therefore, this polymer blend can open new opportunities for the production of devices through additive manufacturing.[79,80] In addition, additive manufacturing has several advantages such as formability, variability, practicability, mass delivery, and surface properties design.[81] Various methods of additive manufacturing have also been developed; for instance, laser melting, laser polymerization, extrusion thermal, material jetting, and material adhesion. Specifically, the PLA is well reported for additive manufacturing,[79,82–85] but SMMA copolymer has null reports in this field.

Moreover, the semi-crystalline PLA, PMMA, and PS have been considered for potential applications in orthopedics, scaffolds, and tissue engineering. The focus has been on cell proliferation, vascularization, shape-memory polymer material; also, appropriate mechanical properties are paired sought.[80,86–92] PLA can be biodegraded under natural body conditions.[93] However, new scaffold architectures can be designed by delaying or anticipating the amorphous PLA biodegradation when PLA is blended with non-biodegradable polymers. On the one hand, the prepolymers of PMMA, PMMA-*co*-PS or their mixtures constitute principal matrix for acrylic bone cement.[94]

The main disadvantage of amorphous PLA (PDLA) is that it has lower properties than semi-crystalline PLA.[83] The key question of the research in this study was whether

a polymer blend between PDLA and SMMA could be made, containing the largest amount of amorphous polymer, presenting a similar Young's modulus to random copolymer, and therefore, the random copolymer improves the processability conditions for additive manufacturing.

In the present contribution, we reported the mechanical, thermal, and rheological properties of amorphous poly(lactide acid) with SMMA copolymer blends via melt mixing process. Equally important, the processing conditions for filament extrusion and its additive manufacturing were established for these blends.

4.2 Materials and methods

PLA Ingeo 4060D, D-lactide 12%, from NatureWorks LLC, USA. The average molecular weight of 190 kg/mol and 1.24 g/cm^3 of density. SMMA, NAS®30, ρ=1.090 g/cm^3, from Ineos Styrolution Group GmbH, Germany.

4.2.1 Blend processing

The amorphous polymer and random copolymer were dried at 60 °C for 8 h. The blending was done using a Brabender internal mixer (BB) [DDRV501, C.W. Brabender Instruments Inc., NJ, USA], at 50 rpm, and 195°C of temperature. Blends compositions are reported in Table 5.1. Afterward, the PLA/SMMA blends were ground through a blade mill to obtain pellet particles and then they were used to produce 3d printing filament and posteriorly to be printed.

4.2.2 Extrusion

The 3D filaments were produced through a self-made single-screw extruder using PLA/SMMA blends pellets. A temperature of 195°C was set. The average filament diameter of the three PLA/SMMA blends was 1.75±0.1 mm.

Table 4.1. Blends compositions of PLA and SMMA copolymer.

Samples	PLA / SMMA (w /w, %)
Neat PLA	100
Neat SMMA	100
$PLA_{50}SMMA_{50}$	50 / 50
$PLA_{75}SMMA_{25}$	75 / 25
$PLA_{80}SMMA_{20}$	80 / 20

4.2.3 3D printing

The adequate properties for additive manufacturing were proved through a CTC 3D printer, at 196 °C. The specific parameters are shown in the corresponding section.

4.2.4 Mold processing

The molding process was realized to test the material probes and then to determine the mechanical properties. The probes were done in a hot plates molding machine model 4122 Bench Top manual press, from Craver®, USA. The molding process was done using PLA/SMMA blend pellets, and pristine PLA and SMMA. Two steps of molding were used: a zero load during 1 min was applied in the first step, and a maximum

load of 2.75 ton at 225°C for 3 min in the second. The probe's dimensions are according to the ASTM D638 Type IV.

4.2.5 Characterization

4.2.5.1 Mechanical properties

To carry out the mechanical testings, a 3382 floor model universal testing system from Instron, USA, was used. A velocity of 5 mm/min was set. The tensile mode was selected, and five probes were evaluated.

4.2.5.2 Rheological properties

A rotational rheometer (Physica MCR 501, Anton Paar) was used. The conditions were: oscillatory mode, parallel plate geometry with a plate diameter of 25 mm, and a gap of 1 mm. The analysis was carried out at a temperature of 195 ºC.

4.2.5.3 Differential scanning calorimetry (DSC) analysis

DSC measurements were carried out in a DSC Q2000 equipment from TA Instruments, USA. A rate of 10 °C/min was used with two cycles: a first heating step at 200 °C followed by a cooling step to 20 °C; then a second heating step at 200 °C finished the testing. Argon environment was used on all samples.

4.2.5.4 Thermogravimetric analysis

Thermal degradation was measured under an air atmosphere with an equipment SDT Q600 from TA Instruments, USA. The PLA/SMMA blends, PLA, and SMMA were heated with a rate of 10°C/min up to 800°C.

4.3 Results and discussion

4.3.1 Mechanical properties

4.3.1.1 Young's Modulus

Figure 4-1a shows Young's modulus of neat polymer, random copolymer, and the PLA/SMMA blends. The values of Young's modulus were 1.57, 1.58, and 1.6 GPa for $PLA_{50}SMMA_{50,}$ $PLA_{75}SMMA_{25,}$ $PLA_{90}SMMA_{20}$, respectively. The increasing effect of Young's modulus values was due to compatibility between the polymer and random copolymer. The terms "compatibility" and "miscibility" have different meaning in polymer blends, the first one making reference to the behavior of the blend in terms of mechanical properties and the second one being related to the formation of a homogeneous system at a molecular level [95]; usually a miscible mixture is compatible, but a compatible mixture is not necessarily miscible. The Young's modulus of PMMA was reported as 3.3 GPa, a higher value than the SMMA used in the present work.[96] It is important to mention that amorphous PLA has lower Young's modulus values than semi-crystalline PLA, with values close to 2 GPa.[93,97]

Young's modulus was improved for PLA/PMMA blends when PMMA was added to the PLA matrix according to literature reports.[98] Also, the PLA used as reinforcement in polymer blends has been reported; for example, polyethylene/PLA blends showed a higher Young's modulus than neat polyethylene when PLA was added.[99] A similar work studied the effect of adding PLA on polyethylene film wasted, reporting an improvement for Young's modulus.[99]

4.3.1.2 Elongation at break (%)

Contrarily to Young's modulus, a decreasing effect on the elongation at break (%) was observed in Figure 4-1b. When SMMA content was reduced in the PLA/SMMA blends, the elongation at break improved. The blend $PLA_{90}SMMA_{10}$ had the highest value of 3.84 %. This same effect was observed on PLA/PS blends.[100] The elongation at break of polystyrene was also reported of about 4.3%[101], a closer value to the present result. An interesting issue is that the elongation at the break override the neat SMMA copolymer when just adding 10 wt % of SMMA into PLA matrix. It was justified the use of low concentrations of the copolymer to get better mechanical properties.

4.3.1.3 Tensile strength

The PLA/SMMA blends also showed compatibility in tensile strength as noted in Figure 4-1c. In general, it is observed that blend $PLA_{90}SMMA_{10}$ presented the highest value (56 MPa), which even surpassed the neat PLA value (52 MPa). The $PLA_{50}SMMA_{50}$ blend has a lower value than SMMA copolymer with a value of 45 MPa. The blend with the lowest value in this property was $PLA_{75}SMMA_{25,}$ suggesting there is an inverse effect

of this tensile strength related to complex viscosity or higher T_g right displacement in thermal properties. The PLA, in some cases, can be used to increase mechanical properties for specific blends.

The addition of PLA to polystyrene (PS) matrix increased the ultimate strength properties due to low interfacial tension and high-stress transfer parameters in the PLA/PS blends.[26] Concerning other similar PLA blends, PLA/PMMA also showed an increasing effect on the tensile strength when adding PMMA fraction on the PLA matrix.[24] Another study reported PLA/polyethylene film wasted blends showing a decreasing effect in elongation at break but a higher ultimate tensile strength was observed according to the results in the literature.[99] An increased value from 232 MPa to 1137 MPa with a weight fraction from 0-0.5 of PLA (3100 HP, NatureWorks LLC, USA) in the matrix was reported. Furthermore, the tensile strength of about 54 MPa was found when carbon nanotubes were incorporated in the PMMA matrix. This value surpassed our results regarding ultimate tensile strength.

4.3.2 Rheological properties

The aspect of miscibility/homogeneity of the binary mixtures was studied through Han and Cole-Cole plots. It is appropriate to state that the Han plot has been used to identify the miscibility of polymer blends [92] at different temperatures and compositions. The Han plots of $PLA_X/SMMA_y$ blends with different random copolymer content at 195 ºC are displayed in Figure 4-2a. A significant characteristic concerning to Han plot (log G' vs log G'') is that a slope of 2 must be observed in the terminal region if a blend is regarded as being truly homogeneous.[102,103] The result of the $PLA_{90}/SMMA_{10}$ slope was the largest

of all the mixtures while $PLA_{50}/SMMA_{50}$ was the lowest. In other words, the miscibility is present in the blends as a function of the PLA content.

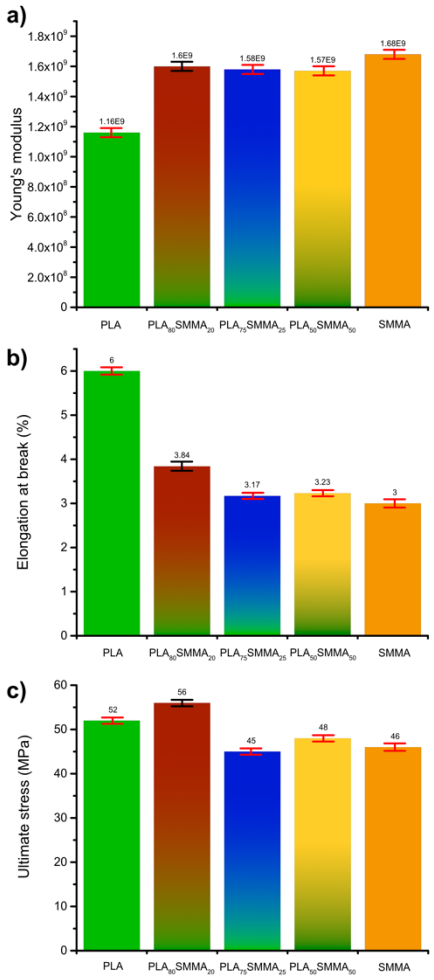

Figure 4-1. a) Young's modulus; b) elongation at break; c) Ultimate stress of PLA, SMMA, and blends.

Furthermore, Figure 4-2b illustrates Cole-Cole plots of all samples. These plots present information about the relaxation process occurring in polymeric blends. In particular, these diagrams are semicircles; if only one circle is observed, is an indication of miscibility, but if two semicircles appear indicates immiscibility.[104] As noted, in the case of PLA and SMMA neat polymers, the Cole-Cole diagrams were circular arcs with

different size, PLA smaller than the random copolymer.[105] The other samples present a single circular arc, suggesting miscibility between PLA and SMMA. However, the blends with high PLA content have closed curves. Ding et al. used Cole-Cole plots and reported two relaxation behaviors in PLA/PBAT blends. In those Cole-Cole plots, two arcs appear: the left arc explains the polymer chain relaxation and the right arc accounts for the droplet relaxation.[106] Similarly, Singla et al. reported excellent compatibility and homogeneity for PLA/EVA blends due to adequate semi-circular curves in Cole-Cole plots. The PLA in that paper had a very similar shape to the present study, and when the content of EVA was of about 30 wt % the curve was opened showing incompatibility behavior.[107] In addition, Maroufkhani et al. observed a tail at the end of the curves in Cole-Cole plots, confirming phase separation between PLA and acrylonitrile-butadiene rubber (NBR).[108] Also, the authors evaluated the slope in the first arcs of the curves, and they reported an excellent uniformity when lower slopes were present in PLA/NBR blends. Adrar et al. reported the effect of adding epoxy functionalized graphene (EFG) to PLA/PBAT blends and observed a semicircular shape showing good miscibility. They also incorporated organo-montmorillonites (OMt) in the blends, and reported a linear behavior in the curve of η'' vs η' due to the filler effect.[109]

Figure 4-3a displays complex viscosity, η^*, the results of amorphous PLA, SMMA, and their blends. Equally important, the effect of amorphous PLA, when incorporated into the blends, is in the viscosity stabilization as a function of frequency. Conversely, a disadvantage of the SMMA is its high η^*, and a small plateau at low frequencies, that is, behavior by shear thinning. It should be noted that the PS and PMMA presents a similar graph of η^* as a function of frequency compared to SMMA, but more identical to the PS

due to a more significant number of styrene monomer units according to the composition of the random copolymer.[110] In particular, the $PLA_{75}SMMA_{25}$ and $PLA_{90}SMMA_{10}$ samples presented a broad plateau in comparison with neat PLA and SMMA copolymer. However, at high frequencies, all materials converge in similar values presented a notable η^* decreasing behavior when reaching approximately 30 Hz.

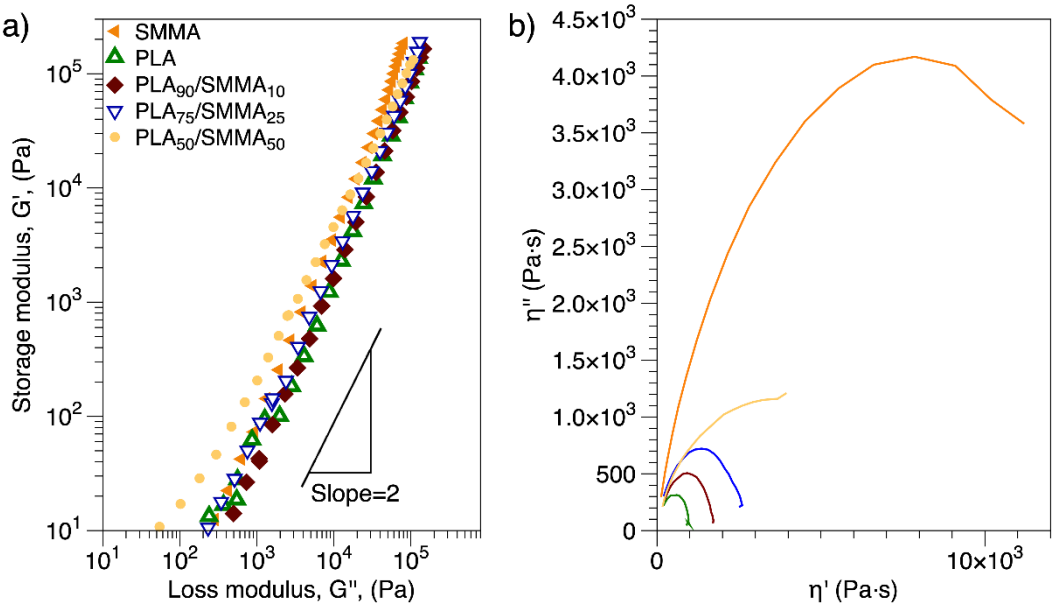

Figure 4-2. a) Han plot of $PLA_X/SMMA_Y$ blends, PLA and SMMA. b) Cole-cole plot of $PLA_X/SMMA_Y$ blends, PLA and SMMA

Likewise, the η^* has been used in polymer blends to identify if there is an interaction that promotes miscibility between the phases or structure changes. For instance, the composites present an increase as a function of the filler content in the polymer blends. [111–114] On the flip side, in this study PLA, and SMMA present differences in their η^* due to their molecular weight, resulting in polymer mixtures with behavior between the frontier of the neat polymers. In summary, the $PLA_X/SMMA_Y$ blends do not show an interaction between the phases that modifies the classic behavior of the polymeric mixtures.

Figure 4-3b shows that PLA/SMMA blends converged at high frequencies, but at lower ones, the blends showed a predominant elastic behavior. The miscibility of a blend is observed by oscillatory rheology where storage modulus is closer to the behavior of a neat homopolymer. The PLA blend showed the lower storage modulus at low frequencies, while the SMMA, had a high value in the same range. From 7 Hz to the highest frequency, $PLA_{75}SMMA_{25}$ presented a higher modulus than $PLA_{50}SMMA_{50}$; as well, for $PLA_{90}SMMA_{10}$ there is a similar situation at 30 Hz approximately. The storage modulus G' decreased with PLA concentration in the PLA/SMMA blends. This same behavior was observed in another blend constituted from PLA-EVA.[107] The correlation of $G' \sim \omega^2$ was observed in our results which supports miscibility and this same behavior coincides with the blends prepared by Zhang et al. with PEO/PMMA blends.[111] In addition, the PVDF/PMMA blends studied by Chiu et al. showed an increase in G' in comparison to neat PMMA. Despite, this PVDF/PMMA G' decreased more than neat PMMA when varying temperature.[112] Similarly, Mao et al. observed an increase for G' in the PMMA/ Chlorinated polyethylene PCE blends, and they attributed this effect to the short time for chains relaxation. Regarding storage modulus, the PMMA/Chlorinated polyethylene(PCE) G' was higher than neat PMMA at low frequencies too.[113] Another work made by Sunil et al. reported shorter values for G' than neat PMMA in polyvinylchloride(PVC)/PMMA blends due to the PVC/PMMA blends with nitrile rubber(NBR) were obtained from recycling.[114]

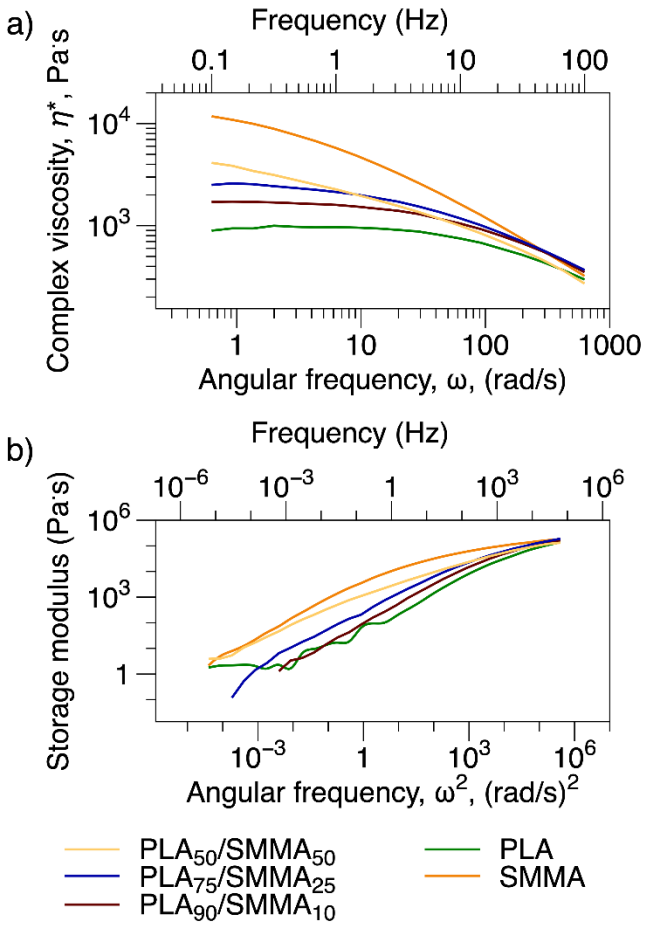

Figure 4-3. a) Complex viscosity; b) Storage modulus of $PLA_x/SMMA_y$ blends, PLA and SMMA

Figure 4-4 shows the behavior of the curves obtained by sweep frequency vs storage modulus (G') or loss modulus (G''). It is well known that G'' dominates over G' at low frequencies, following a typical polymer behavior.[115–117] Furthermore, the crossing point may change according to the composition or the branches generation resulting from the melt mixing of the polymers. Therefore, all $PLA_x/SMMA_y$ blends have the same rheological curves previously described. The crossing point of G' and G'' on PLA, SMMA and their blends were obtained. For the neat PLA, the crossing point of G' and G'' was presented at 457.18 rad/s, while the SMMA crossing point was located at 12.93 rad/s. The $PLA_{50}SMMA_{50}$ blend presented a crossing point of the storage and loss modulus at

about 118.69 rad/s. The crossing point of $PLA_{50}SMMA_{50}$ shifted 70% of the PLA frequency to the left. Contrarily, the $PLA_{90}SMMA_{10}$ had a crossing point of approximately 360 rad/s. Comparatively, the $PLA_{75}SMMA_{25}$ crossing point was observed with higher displacement at 178.07 rad/s. In general, at low frequencies G''>G' shows a fluid state, whereas when G'>G'' exhibits a solid-state behavior.

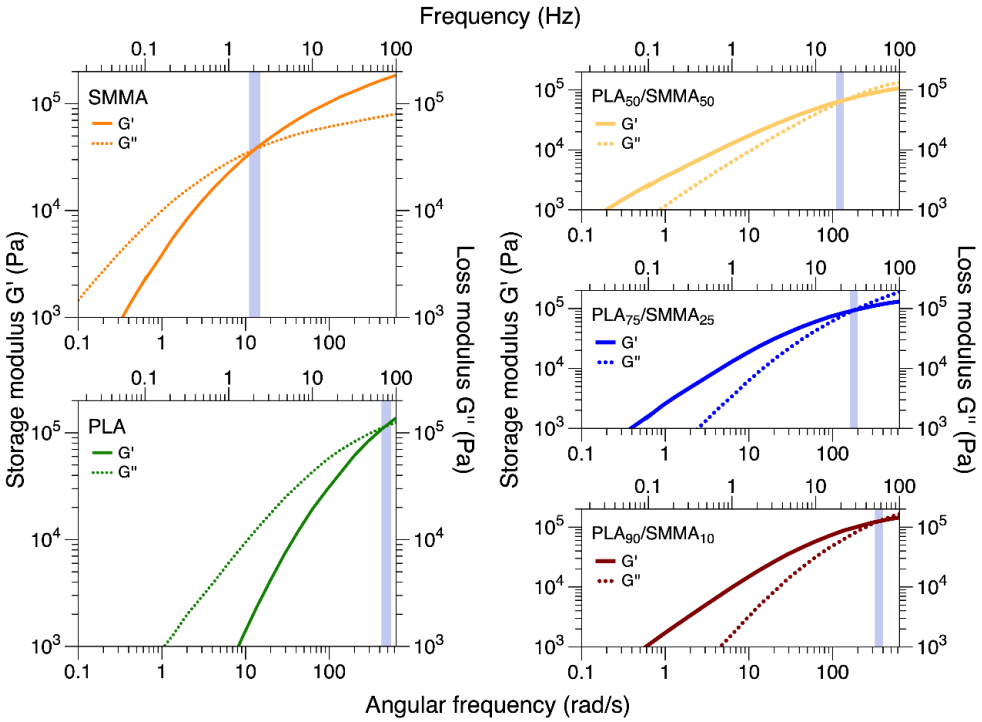

Figure 4-4. Crossing points of $PLA_X/SMMA_Y$ blends, PLA and SMMA

4.3.3 Thermal properties

4.3.3.1 Differential scanning calorimetry

Miscibility explains a good interaction among polymers concerning polymer blends, once two polymers have been blended and if there are the corresponding individual T_g values, it means immiscibility is present. Otherwise, if a single transition glassy temperature is observed, miscibility can be assumed.[118] On the other hand, a different situation in another work was reported, where a slight T_g displacement on PLA/PS blends suggested compatibility for those blends.[100] Figure 4-5 shows the thermogravimetric curve obtained in differential scanning calorimetry. In general, all PLA/SMMA blends showed higher $T_{g's}$ of polymer and random copolymer. These results suggest immiscibility because both T_g's remain in the binary blend, but compatibility due to mechanical properties. In another work, a single T_g for semi-crystalline PLA/PMMA blends varying compositions of PMMA on PLA matrix supported the miscibility term.[98] Opposed to it, PLA/PMMA blends miscibility was evaluated with two different methods: 1) solution/precipitation, and 2) solution-casting film. The results showed that for solution/precipitation a single T_g was observed, but two isolated T_g were present in the solution-casting film method.[118] The explanation of this difference concerning T_g about miscibility and immiscibility for these systems is that the first method included both polymers in solution, which favored the spontaneity of free Gibbs energy to form a good blending between polymers causing a single T_g of the system, whereas the solution-casting needed energy to produce a proper polymer blend due to the presence of just one polymer in solution.

One advantage of this kind of polymer blend is that there are no semi-crystallinity phases in the polymer blend, which represents an interesting and low energetic processing for the production of this material. The dominating phase in the system is attributed to the PLA due to the high composition in the blend and also because this phase has the lowest glass transition temperature (57.16 °C). During filament production stage the PLA phase is above rubber state andit allows the flow mostly of the polymer blend being stabilized by the copolymer, which has a higher Tg of about 100.4 °C. The amorphicity of the system does not depend on the heating and cooling rates facilitating the 3d printing process and it can be an expetional processing condition when comparing the use of amorphous PLA and semi-crystalline PLA.

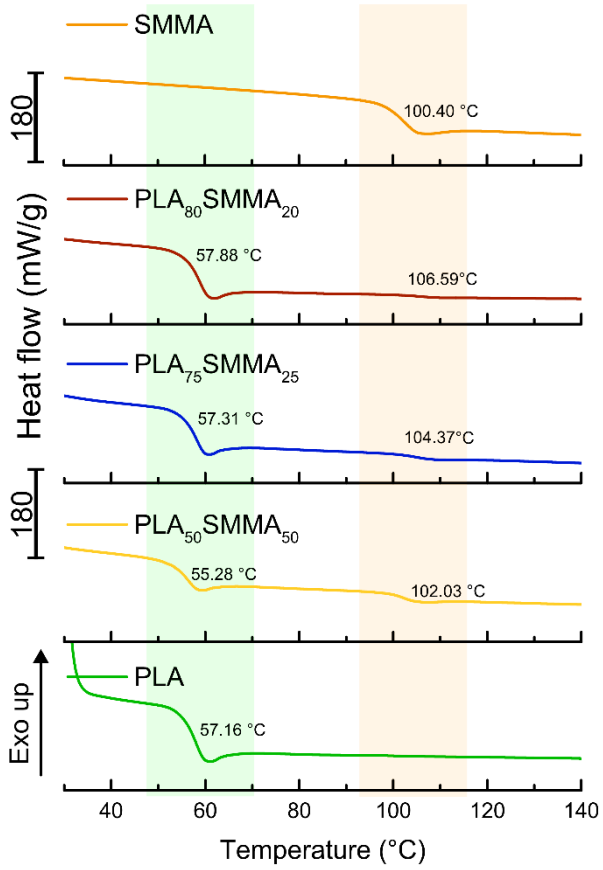

Figure 4-5. Glass transition temperature of $PLA_X/SMMA_Y$ blends, PLA and SMMA

4.3.3.2 Thermogravimetric analysis

Figure 4-6 shows the thermogram of PLA, SMMA and PLA/SMMA blends. An interesting behavior was observed where mostly all blends had two maximum degradation temperatures. These two maximum peaks are in agreement with other research works as for example PLA charged with ceramic nanocomposites and another concerning phosphorous-PLA composites, respectively.[119,120]

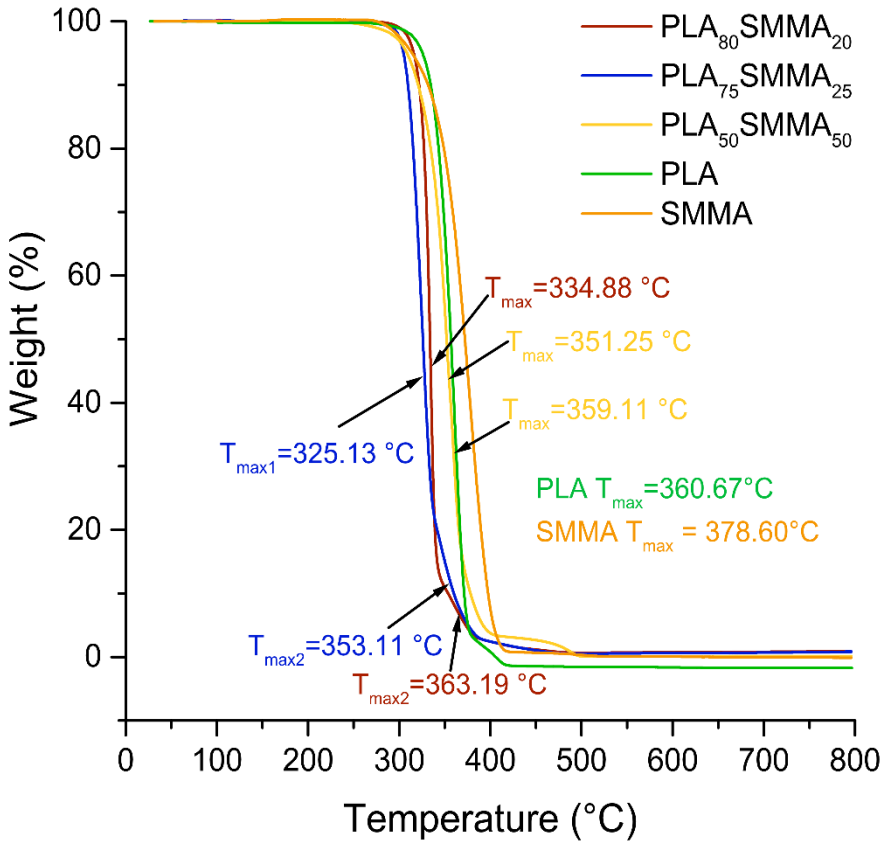

Figure 4-6. Thermogram of $PLA_X/SMMA_Y$ blends, PLA and SMMA

4.3.4 Filament extrusion and 3D printing

The addition of the random copolymer to the blends was for evaluating the material under processing conditions (filament production and 3d printing). As well as, develop the methodology, specifically for the amorphous PLA because it has lower mechanical properties than its semi-crystalline counterpart. In general, these blends present Young's modulus like the SMMA copolymer, but a decrease in the elongation at break and tensile strength were observed. In like manner, the best polymer blend was $PLA_{90}SMMA_{10}$ concerning the mechanical properties.

Moreover, the filaments of the three PLA/SMMA blends were produced via extrusion. The equipment was designed with two heating zones, a single screw, and a nozzle, where the nozzle output has a diameter of 1.75 mm. The angular velocity found in the screw extruder was equal to that complex viscosity observed in the oscillatory test, and, this allowed the proper filament extrusion. The range of temperature of the heating sources was of 150°-240°C, where the appropriate extrusion temperature for PLA/SMMA blends was set at 196°C in the barrel and nozzle frontier.

The $PLA_{90}SMMA_{10}$ blend was selected to show the 3D printing process in the present work. Uniform diameter of 1.75 mm was reached, this size was also well reported in other works.[86,121] However, another diameter of 1.6 mm was reported for PLA-hydroxyapatite filaments.[85] The printing temperature is normally set between 180-240 °C for blends and composites having PLA as a matrix. For example, in a few works, 210 °C were used when printing PLA,[85,122] but also, a lower temperature of 190°C was set in another work.[36] The proper filament was charged to a CTC 3D printer. In Table 4.2 3D printing parameters are displayed. A small cube of 2 cm per side was used as a model.

Table 4.2. Parameters of 3D printing

Parameter	**Value**	**Units**
Object infill (%)	10	%
Layer Height (mm)	0.25	mm
Number of shells	3	
Feed rate (mm/s)	30	mm/s
Travel feed rate	35	
Print temperature (°C)	196	°C

4.4 Conclusions

Compatibility was verified by improving Young's modulus for the $PLA_{50}SMMA_{50}$, $PLA_{75}SMMA_{25}$, and $PLA_{90}SMMA_{10}$ blends. The $PLA_{90}SMMA_{10}$ blend showed the highest value for tensile strength and elongation at break (%) due to the incorporation of the acrylic to the polyester phase. The rheology showed an improvement in complex viscosity for all blends and copolymer when compared with neat PLA. In addition, when higher PLA concentration was in the PLA/SMMA blends, the complex viscosity decreased. Concerning the crossing point of storage (G') and loss (G'') modulus the $PLA_{75}SMMA_{25}$ blend showed a displacement to the left, almost reaching the neat SMMA crossing point. All PLA/SMMA blends showed two glass transition temperatures closer to neat polymer and copolymer initial values, and this suggested compatibility in the system. The thermal property of the PLA/SMMA blends showed lower maximum decomposition temperatures when compared with the PLA and SMMA.

A successful filament for 3D printing was obtained, with a uniform diameter of 1.75 +/-0.1mm. Lastly and more importantly, the 3D printing was carried out, leaving the present material to new 3D printing applications. The PLA has demonstrated to be noble for the 3D printing process, so this study aimed to have a higher composition of PLA than SMMA.

CHAPTER 5. TERNARY POLYMER BLENDS PLA/PA/SMMA

5.1 Introduction

Polymer blends are intended to produce new properties, improved, and supported for a specific application. The evidence of these new properties generally acquired to benefit some of the polymer components in the blend and originated from the blending process defining the compatible or incompatible terms.[95] Poor mechanical properties are found in polymer blends, due to the high interfacial tension[123] and also from the thermal degradation they experience.[124] Polymer blends represent new materials as an alternative, conformed from synthetic and biodegradable polymers intended for packaging.[125] These materials can be found in the biomedical field, opening the mechanical material behavior and its processing under different procedures. For the present study, three polymers were considered: poly (lactide acid) (PLA), poly (styrene-co-methyl methacrylate) (SMMA) and nylon 6 (PA 6).

PLA could be blended with other polymers as polycaprolactone (PCL) and hyaluronic acid (HA) for tissue Engineering.[126] Also, blends such poly (lactide acid) (PLA)/ poly (ethylene glycol-diacrylate) (PLA/PEGDA), poly (lactide acid) (PLA)/poly (propylene-glycol) (PLA/PPG), poly (lactide acid) (PLA)/ poly (butylene-adipate-*co*-terephthalate) (PLA/PBAT) with ADR-4370S chain extensor.[127]

Polyamide blends are used in the biomaterials field research. For example, the study of a new matrix comprised of PA 12 and polyethylene for nano-hydroxyapatite (nHA), resulting in a porous structure intended to bone process regeneration.[128] One of the main characteristics of polyesters as PLA, is the biodegradability property, owned to

the cleavage of the ester group. Contrarily, polyamides do not present that behavior due to the hydrogen bonds in the individual chains. [129] Similarly, there is a research work of a chitosan-PA 6,6 blend produced via electro-spinning, which occasioned the increasing of the elastic modulus of the blend at different compositions.[130] To blend different origin source polymers has attracted a research group, which studied the shape-memory effect in poly (lactide acid) PLA/ poly (methyl methacrylate) (PMMA) blends, and where an interesintg behavior of elastomeric-type material conformed in the blend was observed through the heat external application.[131] An adequate structure for drug delivery application also was reported in these blends (PLA/PMMA).[132] The crystallization in copolymer constituted from styrene and methyl methacrylate units also has been investigated. For example, the crystallization rate was reported for blends of poly (lactide acid) (PLA) and poly (styrene)-*b*-poly (methyl methacrylate) (PS-b-PMMA) showing polymorphism among blends.[133]

It results interesting to produce new polymer blends, departing from polymers proved in the medical field. Before to think in final products, there is a need for knowledge about the interaction in ternary blends whose include PA 6. The present study intends is to show a new ternary polymer blend PLA-SMMA-PA 6, first time reported, with potential application in the medical field.

5.2 Materials and methods

PA 6 national polymers PLA Ingeo 4060D, D-lactide 12%, from NatureWorks LLC, USA. With an average molecular weight of 190 kg/mol and 1.24 g/cm^3 in density. PLA amorphous was selected differentiating in the previous studies mentioned, which mostly,

have used semi-crystalline PLA. Poly (styrene-co-methyl methacrylate (SMMA), NAS®30, ρ=1.090 g/cm^3, a copolymer is belonging to Ineos Styrolution Group GmbH, Germany. It was used as the second thermoplastic to compose the binary blending system. PA 6 from National Polymers, Mex., with a density of 1.08 g/cm^3.

5.2.1 Blending processing

Three neat polymers and six blends were dried at 60°C for 12 h, the adequate mixing was carried out using a Brabender internal mixer (BB) [DDRV501, C.W. Brabender Instruments Inc., NJ, USA], at 50 rpm, and a set temperature of 235°C. 50 g were used in the mixing chamber by sample.

Table 5.1. Samples compositions of ternary polymer blends $SM_xPA_yPLA_z$

ID sample	Poly (styrene-*co*-(methyl-methacrylate) (SMMA), w/w	Polyamide 6 (PA), w/w	Poly (lactide acid) (PLA), w/w
$SM_{50}PA_{30}PLA_{20}$	50	30	20
$SM_{80}PA_{10}PLA_{10}$	80	10	10
$SM_{70}PA_{20}PLA_{10}$	70	20	10
$SM_{10}PA_{10}PLA_{80}$	10	10	80
$SM_{20}PA_{10}PLA_{70}$	20	10	70
$SM_{30}PA_{20}PLA_{50}$	30	20	50
SMMA	100	0	0
PA6	0	100	0
PLA	0	0	100

5.2.2 Characterization

5.2.2.1 DSC Characterization

Differential scanning calorimetry was carried out with the DSC Q2000 from TA Instruments, USA. The rate of heating-cooling was 10°C/min contemplating two cycles: heating samples at 200°C, then cooling reaching 20°C, and again heating up to 200°C; atmosphere: Argon.

5.2.2.2 Thermogravimetric analysis

Thermal degradation was measured with Instrument SDT Q600 TA Instruments, USA. The same heating rate was used at 10°C/min. Atmosphere: Air.

5.2.2.3 Rheological properties

A rotational rheometer (Physica MCR 501, Anton Paar) on oscillatory mode and using parallel plate geometry: Ø= 25 mm and a gap of 1 mm, run at 225°C.

5.2.2.4 Mechanical properties

To carry out the mechanical testing's, A 3382 Floor Model Universal Testing System from Instron, USA, was used. A velocity of 0.5 mm/min was set. The tensile mode was selected.

5.2.2.5 Infrared spectroscopy

A Nicolet Magna 750-IR spectrometer was used to obtain the blends spectra. Then the signals were deconvoluted by using a Gaussian method.

5.3 Results and discussion

5.3.1 Thermal properties

5.3.1.1 Thermogravimetric analysis

Figure 5-1 shows the thermogravimetric curve of mass loss and derivative versus temperature function. During TGA analysis it can be observed at 240 °C and below that, individually, the PA 6 is the polymer which losses more mass than PLA and SMMA with a maximum mass loss of 1.6 % at 245 °C. PLA and SMMA loss a maximum mass of 0.2 %. This mass loss observed through TGA eliminates the possible thermal degradation among three polymers in ternary blends (Figure 5-1).

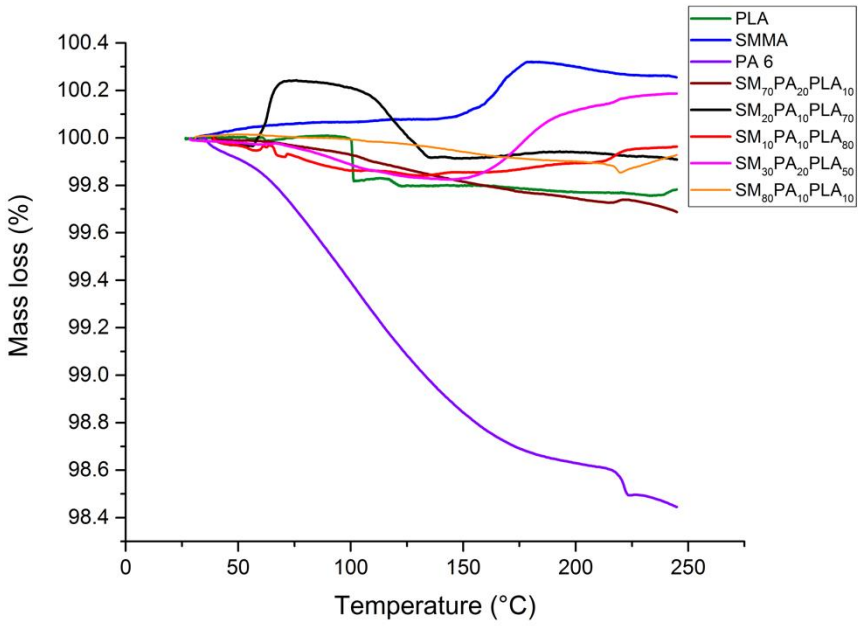

Figure 5-1 General mass loss curve of neat polymers, copolymer and samples

It is well reported PA 6 has maximum degradation peaks at 450, 446, and 397°C;[134] [135] [136] which fits well in the present thermogravimetric curves. It can be observed in the derivative of mass over temperature that PLA has a faster thermal decomposition than SMMA and PA 6. PLA showed a maximum temperature peak at 360.5 °C, whereas SMMA and PA 6 had 377.7 and 453.20 °C respectively. In the case of blends under 50 wt % of copolymer SMMA degradation occurs before neat PLA (Figure 5-2). For these blends derivative decreases in the following order: $SM_{10}PA_{10}PLA_{80}$, $SM_{20}PA_{10}PLA_{70}$, $SM_{30}PA_{20}PLA_{50}$. On the contrary, when SMMA composition is above 50 wt % the degradation temperatures appear after the PLA degradation. Two blends: $SM_{80}PA_{10}PLA_{10}$ and $SM_{70}PA_{20}PLA_{10}$ have one peak and one shoulder in the derivative function.

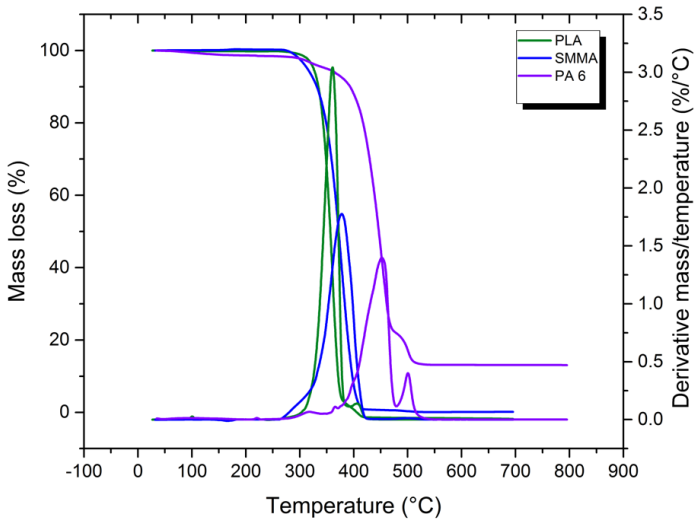

Figure 5-2 General thermogravimetric curve of neat polymers, copolymer and samples

By analyzing these two last blends ($SM_{80}PA_{10}PLA_{10}$ and $SM_{70}PA_{20}PLA_{10}$) in Figure 5-3, we can see the blends with 10 wt % of PLA present different behavior when they

change PA 6 composition. It indicates PA 6 influences also by changing the shoulders between similar blends with compositions of PLA and SMMA. In another research, where Nano-composites in a PA 6 matrix were added, the derivative was reported to be increased. [136] In the present study also there are higher temperature peaks in ternary blends, but these peaks appear at higher temperatures than those used in the mixing and molding processes.

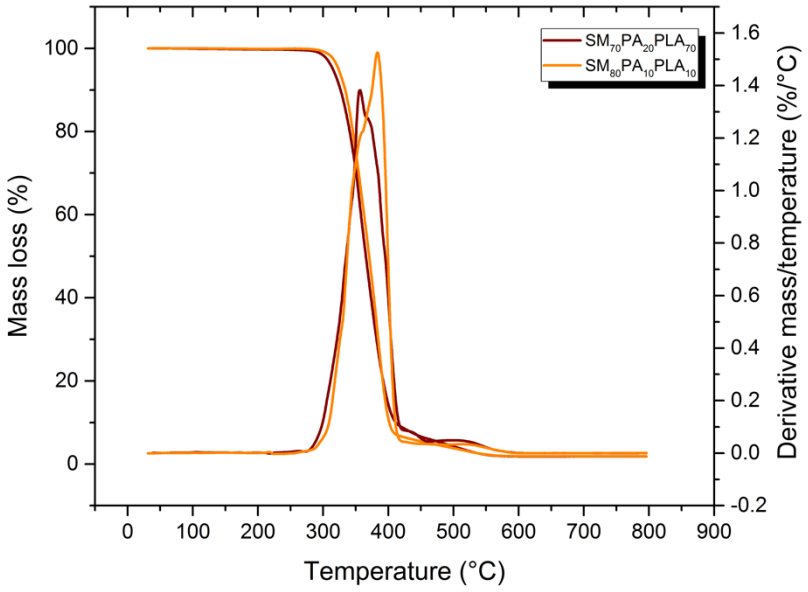

Figure 5-2 Maximum temperature peaks between $SM_{80}PA_{10}PLA_{10}$ and $SM_{70}PA_{20}PLA_{10}$

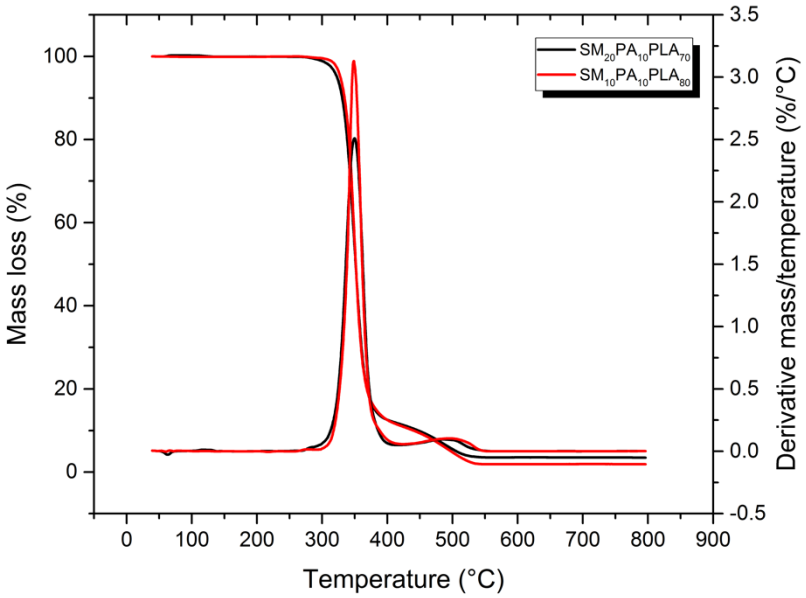

Figure 5-*4* Thermogram showing maximum temperature peaks of $SM_{10}PA_{10}PLA_{80}$ (red), $SM_{20}PA_{10}PLA_{70}$ (black)

5.3.2 Differential scanning calorimetry

Glass transition temperature

In a general behavior, the glass transition temperature (T_g) in the blends is slightly right displaced (Table 5.2) during second heating. As the ternary blend is composed of two amorphous polymers and another semi-crystalline, there are three T_g 's and one T_m (PA 6). As the T_g of the PA 6 (51°C) is very close to that shown by PLA (57°C), there is just one present due to an average T_g in the range that comprises both polymers. The second glass transition temperature is explained by the SMMA T_g alone (100°C). Other research papers report similar values [137], [138], [139]. In Figure 4 there are transition temperature

changes. Three blends have higher values $SM_{10}PA_{10}PLA_{80}$, $SM_{30}PA_{20}PLA_{50}$, and $SM_{20}PA_{10}PLA_{70}$, which means interactions are present. Also, for the SMMA, an increasing T_g is being the highest values in the same blends before mentioned. Once the SMMA composition reaches values up to 50 wt % the T_g's start to decrease more visible for de PLA (it T_g falls 2-5 Celsius on the averages). Also, when comparing first and second heating cycles during dsc testing, the T_g's of the samples in second heating had a more T_g leftwards displacement (Figures 5-5,5-6)

Table 5.2. Glass transition temperatures of ternary polymer blends $SM_xPA_yPLA_z$

Blend	**Tg_1 (°C)**	**Tg_2 (°C)**
PA	51	
SMMA	100.4	
PLA	57.1	
$SM_{80}PA_{10}PLA_{10}$	53.3	100
$SM_{50}PA_{30}PLA_{20}$	56.8	104
$SM_{30}PA_{20}PLA_{50}$	59.5	104
$SM_{20}PA_{10}PLA_{70}$	63	107.8
$SM_{10}PA_{10}PLA_{80}$	58.6	106.7
$SM_{70}PA_{20}PLA_{10}$	55.3	100

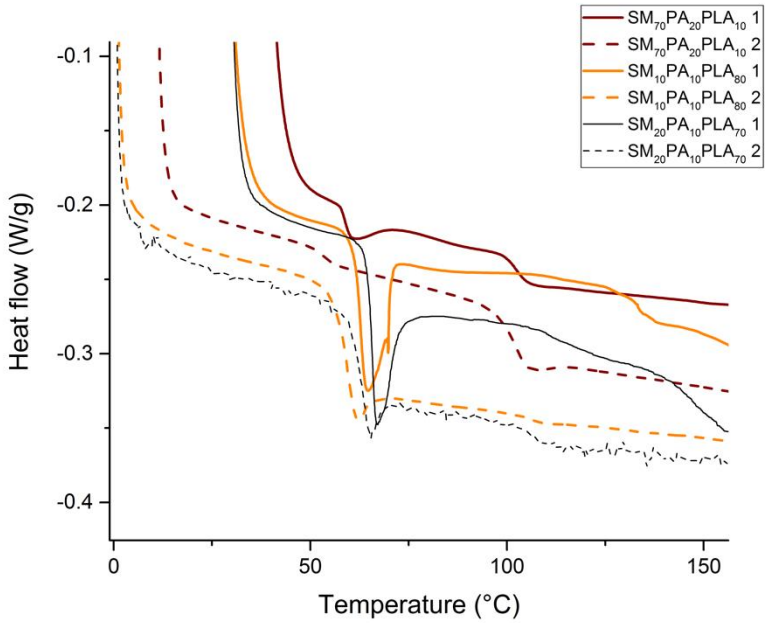

Figure 5-5 Comparison of first and second heating cycles and glass transition temperatures of $SM_{70}PA_{20}PLA_{10}$ and $SM_{20}PA_{10}PLA_{70}$

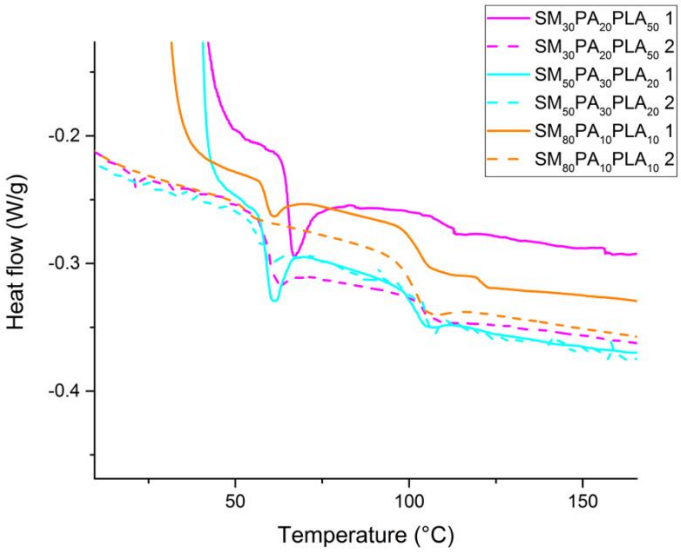

Figure 5-6 Comparison of first and second heating cycles and glass transition temperatures of $SM_{30}PA_{20}PLA_{50}$, $SM_{50}PA_{30}PLA_{20}$, $SM_{80}PA_{10}PLA_{10}$

The PLA and PA 6 pass from glassy to rubbery state when departing from their T_g's towards higher temperatures, however the SMMA copolymer is still in the glassy state because its T_g=100.4 °C. Once the copolymer and homopolymers are about 180°C PLA and SMMA are in a melt state, whereas PA 6 is still in rubbery. At this stage PLA and SMMA can flow, and they become the major phase with amorphous configuration and PA 6 is a rigid domain phase in the ternary system. Once the temperature has attained 222.7 °C, PLA, SMMA and PA 6 are in melt state at the same time.

Crystallization *temperature (T_c)*

There are three types of crystallization in polymer science. The first one is called Melt-crystallization which obeys to the process of arrange crystals from melting to cooling process. A second type is the cold-crystallization which is presented in polymers during heating. Lastly, there is the so called "recrystallization organization" which is explained when there are both steps involved together: heating a small crystal to be melted and then again a second heating process to get bigger or order crystals. [140] In the present study there are no peaks of cold-crystallization. However, the PA 6 does crystallize lastly with respect the rest of the blends in general during cooling at first cycle (Figures 5-7,5-8). This promt crystallization can be attributed to the facilites granted by the amorphous configurations of the PLA and SMMA copolymer in the ternary blend in the melt state, thus the composition of PA 6 in the blend can start to crystallize because there are no other crystals interfering in the crystallization process. Two T_c's were observed for the

$SM_{20}PA_{10}PLA_{70}$ blend reflecting a possible effect of polymorphism very particular of the PA due to the sensitivity to isothermal cooling in DSC testings (Figure 5-7).[141]

Generally, it has been reported that there is no motion of the T_c when immiscibility is present between polymers in polymer blends. [139] This motion can be explaining a partial miscibility in the ternary system, specially supported by the glass transition which is also being displaced. The phase dispersed in the melt state for ternary system should be PA 6, while PLA and SMMA, with amorphous domains as main matrix with amorphous configuration. Table 5.3 shows the crystallization temperatures of the ternary blends.

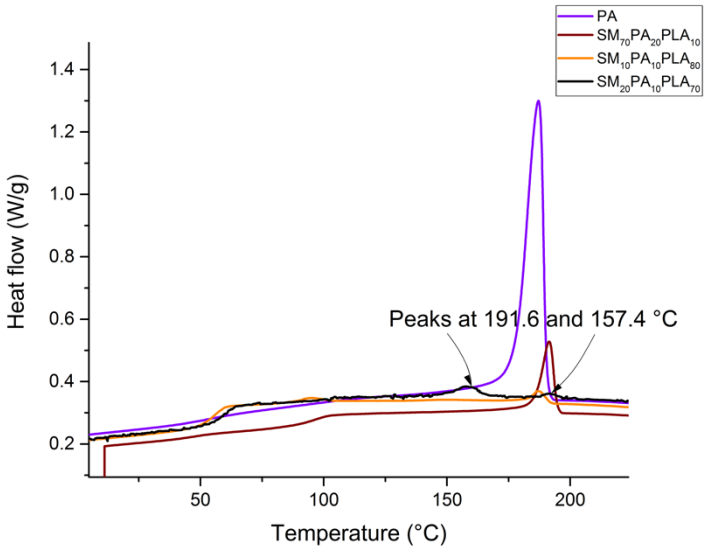

Figure 5-7 Crystallization peaks of $SM_{70}PA_{20}PLA_{10}$, $SM1_0PA_{10}PLA_{80}$, and $SM2_0PA_{10}PLA_{70}$

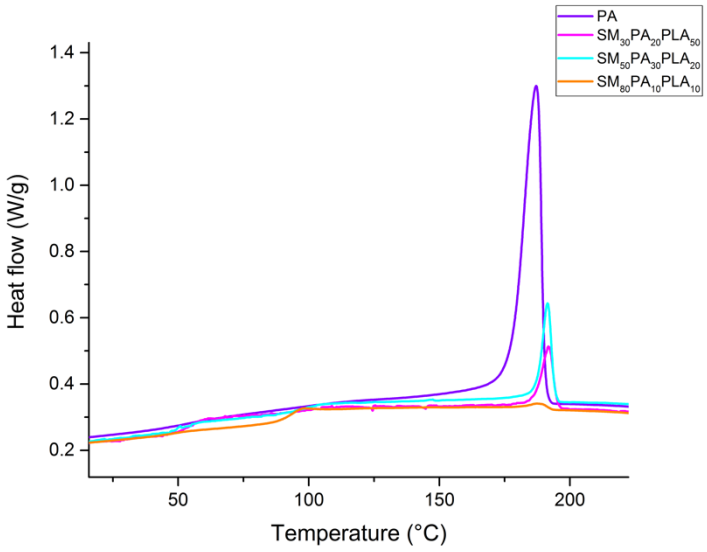

Figure 5-8 Crystallization peaks of $SM3_0PA_{20}PLA_{50}$, $SM_{50}PA_{30}PLA_{20}$, and $SM_{80}PA_{10}PLA_{10}$

Table 5.3. Crystallization temperatures of ternary polymer blends $SM_xPA_yPLA_z$

Blend	**T_c (°C)**
PA	187
$SM_{80}PA_{10}PLA_{10}$	188
$SM_{50}PA_{30}PLA_{20}$	191.8
$SM_{30}PA_{20}PLA_{50}$	191.9
$SM_{20}PA_{10}PLA_{70}$	191.6, 157.4
$SM_{10}PA_{10}PLA_{80}$	187.1
$SM_{70}PA_{20}PLA_{10}$	191.6

The semi-crystallinity of the PA 6 is about 35, 29 % according to other research works.[142,134] To the present study a one-hundredth of semi-crystallinity stays for 53.35 W/J in fusion heat. Table 5.4 shows the semi-crystallinity of the ternary blends. Terms

were obtained by using the enthalpy fusion of the blend divided by the analogous of the neat PA 6 and dividing this quotient by the mass fraction of the PA 6 in the ternary blend.

Table 5.4. Ternary blends and their semi-crystallinity

Blend	Fusion heat (J/g)	X_c (semi-crystallinity %)
PA	53.35	100
$SM_{80}PA_{10}PLA_{10}$	1.53	2.86
$SM_{50}PA_{30}PLA_{20}$	8.38	15.70
$SM_{30}PA_{20}PLA_{50}$	6.34	11.88
$SM_{20}PA_{10}PLA_{70}$	2.55	4.77
$SM_{10}PA_{10}PLA_{80}$	1.32	2.47
$SM_{70}PA_{20}PLA_{10}$	8.14	15.25

Melting point

The polyamide 6 had two melting points during first heating cycle, these were present at 225.4 and 227.8 °C. These two melting points in PA blends are reported in a work of PA with polyvinylidene (PVDF) with one set at 215°C and another at 221°C.[142] After the second heating polyamide 6 showed one T_m at 222.7 °C ,[139] which supports the present results. of the same manner, the heat flow variation was more pronounced in the second heating than during first one. It does mean that thermal variations affected the configuration of PA 6. The melt state is delayed when observing the curve at first heating (Figure 5-9). Two processing temperatures were applied in the ternary blends. The mixing temperature was set at 235 °C, whereas the molding process was done at 240°C. Therefore, both temperatures determined a melt state and no semi-crystallinity was attributed during processing. Similarly, all ternary samples showed a lower melting point in the second heating cycle (Figures 5-10,5-11). There could be an amorphous matrix

conformed of PLA and SMMA with specific compositions for each blend and also there would be a semi-cristallinity domain due to the presence of PA 6. The $SM_{20}PA_{10}PLA_{70}$ probably can have two domains, one with crystals melting at lower temperature and other domains with higher melting points. The melting points of PA 6 and ternary polymer blends are displayed in table 5.5.

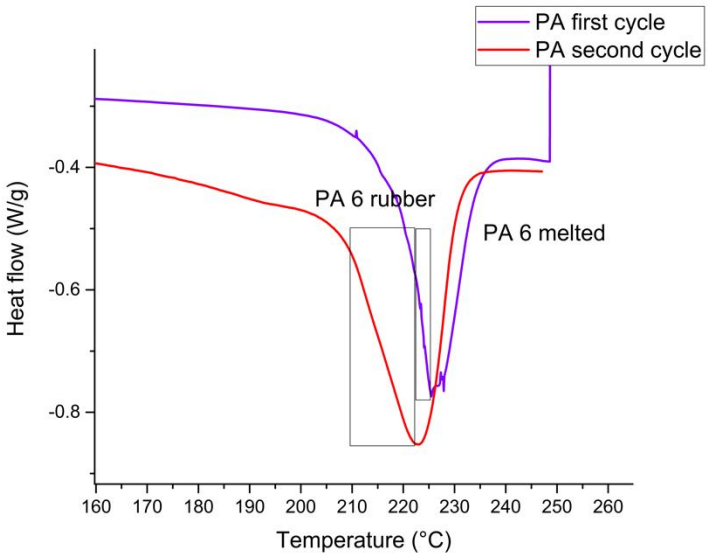

Figure 5-9 melting point at two heating cycles of polyamide 6

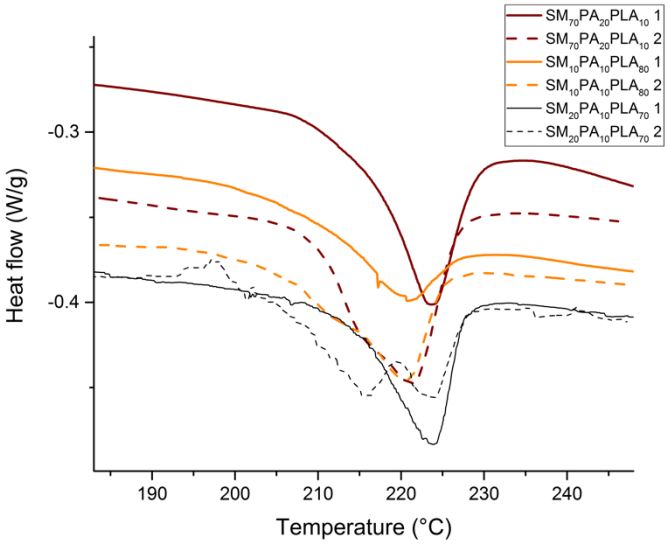

Figure 5-30 Melting point of $SM_{70}PA_{20}PLA_{10}$ and $SM_{20}PA_{10}PLA_{70}$

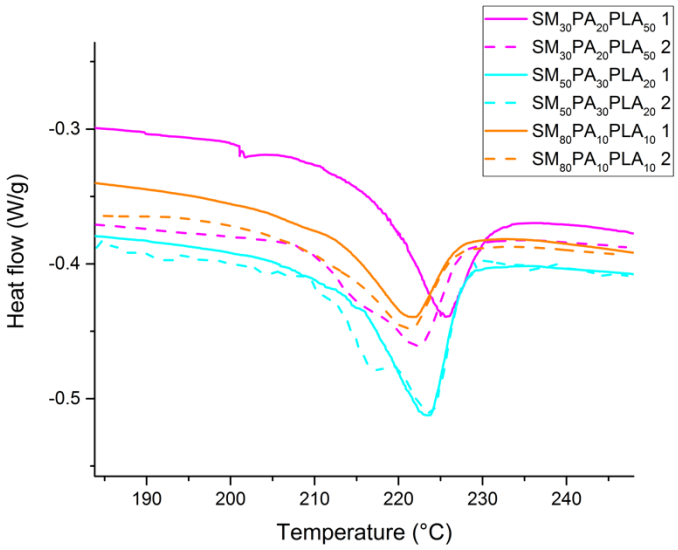

Figure 5-11 Melting point of first and second heating cycles of $SM_{30}PA_{20}PLA_{50}$, $SM_{50}PA_{30}PLA_{20}$, $SM_{80}PA_{10}PLA_{10}$

Table 5.5. Melting points of PA 6 and ternary polymer blends

Blend	T_m (°C) first cycle	T_m (°C) second cycle
PA	225.4, 227.8	222.7
$SM_{80}PA_{10}PLA_{10}$	221.6	221.5
$SM_{50}PA_{30}PLA_{20}$	216.0, 223.2	223.7
$SM_{30}PA_{20}PLA_{50}$	225.7	216, 222.4
$SM_{20}PA_{10}PLA_{70}$	223.6	215.8, 223.5
$SM_{10}PA_{10}PLA_{80}$	221.1	220.8
$SM_{70}PA_{20}PLA_{10}$	223.7	221.2

5.3.3 Rheology

5.3.3.1 Shear rate-shear stress curve

Other authors have reported PLA viscosity, it depends on the PLA configuration type and the work conditions. It is possible to find a higher PLA viscous with 1000 Pa.s [143] and a complex viscosity of 3000 Pa.s [144]. For PA 6 also are reported diverse values 400 Pa.s [145], 200 Pa.s [146]. In the present work, the viscosities individually of PLA, PA 6 and SMMA are 88, 3657 and 2043 Pa.s. As the shear-stress test was conducted at 235 °C it can be inferred the PLA, SMMA and PA 6 are in a melt state. A broad plateau was also observed in almost all blends, with exception of $SM_{50}PA_{30}PLA_{20}$ and $SM_{50}PA_{30}PLA_{20}$ whose plateu regions are shorter. As it was mentioned in TGA section, there is no thermal degradation by temperature exceeding more than 0.3 % of mass loss, which indicates the blends can have a good procesable viscosity without thermal degradation.

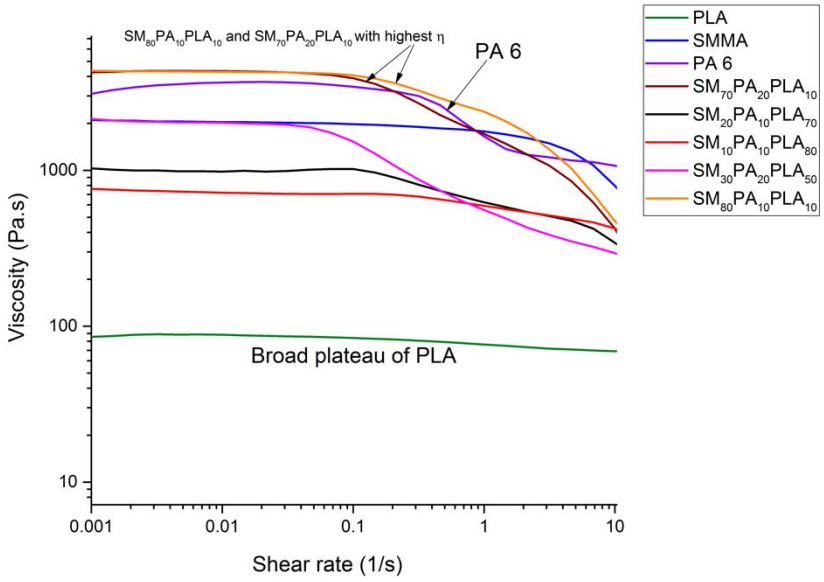

Figure 5-12 Viscosity curve of PLA, SMMA, PA 6 and ternary polymer blends

As shown in Figure 5-12, PA 6 stays with the highest viscosity in the order of 0.3 (1/s), being followed by SMMA with 1100 Pa.s and then PLA with the lower viscosity plateau. It is exciting that all blends surpass the PLA viscosity plateau, being the samples $SM_{80}PA_{10}PLA_{10}$ and $SM_{70}PA_{20}PLA_{10}$ those bends exceeding the PA 6 viscosity. This behavior of viscosity improving is attributed to a new possible Hydrogen bond in the ternary blends. Polyamides can present these types of interactions also in an individual manner by the amine group.[147]

5.3.4 Mechanical properties

The PA 6 is a polymer which possesses excellent mechanical properties. Its elongation at break in tension is reported about 30% and its strength of 70 MPa.[136] The PLA has lower mechanical properties than PA 6, having Young's modulus range of 1-4

GPa, a tensile strength of 40 MPa and the elongation break is reported in 2-6%, (Table 5.3).[89,90, 148,87] For the SMMA copolymer the literature is scarce, and we can cite a work reporting just tensile strength as main property.[149] To evaluate a possible change in the mechanical property, the following blends were prepared to be tested: $SM_{20}PA_{10}PLA_{70}$, $SM_{30}PA_{20}PLA_{50}$, $SM_{50}PA_{30}PLA_{20}$. Table 5.6 shows the mechanical properties of PLA, SMMA, PA 6 and ternary blends.

Table 5.6. Mechanical properties of PLA, SMMA, PA 6 and ternary blends

Blend	Maximum stress	Elongation at break (%)	Young's modulus (GPa)
Neat PLA	52	6	1.16
Neat SMMA	46	3	1.66
Neat PA 6	60	16	2.10
$SM_{30}PA_{20}PLA_{50}$	36.44 Mpa	3.25	4.10
$SM_{50}PA_{30}PLA_{20}$	31 MPa	2.45	3.87
$SM_{20}PA_{10}PLA_{70}$	37.41 MPa	3.79	3.99

5.3.5 IR spectroscopy

Polyamide research works have also reported hydrogen bondings in polymer blends with other polymers. For example, poly(vynil butyral) (PVB) and PA 6 were blended and studied presenting good improvements in thermal decomposition and impact strength for PVB/PA 6 blends. The three polymer structures are schematically showed in Figure 5-13. As previously reported in another research work.[150] The carboxyl groups present in each one of both polymers are interacting with the polyamide Hydrogens. Also, hydrogens are interacting with the N-H group in PA 6. In the present study, the interactions can easier occur due to the chemical structures of the species (Figure 5-14).

This hydrogen bondings can improve the mechanical properties as will be discussed later in the mechanical properties section.

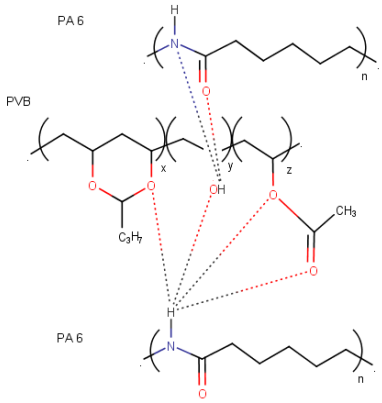

Figure 5-13 PA 6/PVB interactions through Hydrogen bonds

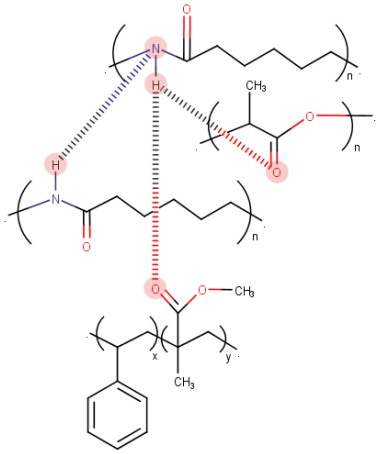

Figure 5-14 Hydrogen bonds among ternary blends in the present study

5.3.6 Mechanical properties with strain gauges

5.3.6.1 Tension

The PA 6 is a polymer which possesses excellent mechanical properties. Its elongation at break in tension is reported about 30% and its tensile strength of 70 MPa [136]. The PLA has lower mechanical properties than PA 6, having Young's modulus range of 1-4 GPa, a tensile strength of 40 MPa and the elongation break is reported in 2-6%.[87,89,90,148] For the SMMA copolymer, the literature is scarce, and we can cite a work reporting just tensile strength as main property.[149] To evaluate a possible change in the mechanical property the following blends were prepared to be tested: $SM_{20}PA_{10}PLA_{70}$, $SM_{30}PA_{20}PLA_{50}$, $SM_{50}PA_{30}PLA_{20}$. Among these blends, the higher properties of Young's modulus, maximum stress, and elongation at break (%) were those belonging to blend SM20PA10PLA70. E=3.88GPa, Smax= 29.4MPa and **ε**=0.8%. The strain-stress curve is shown in Figure 5-15. This depicts a brittle behavior to a tensile test.

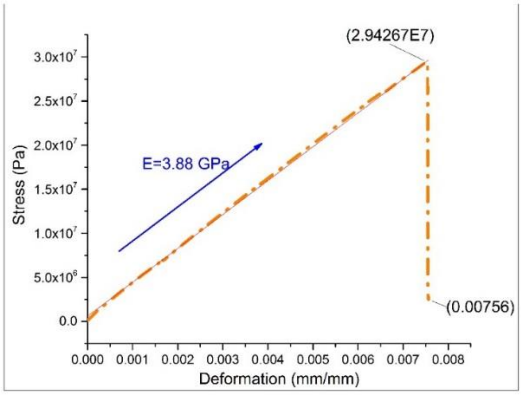

Figure 5-15 Strain-stress curve for $SM_{20}PA_{10}PLA_{70}$ under tension

5.3.6.2 Compression

The behavior of the material under compression showed a plasticizing effect. A maximum load of 8000 N was obtained in the elastic zone. This value covers perfectly the compressive forces acting on lumbar vertebrae. Also, the yield stress had a value of about 70 MPa. The compressive strength of PLA has been reported in other works. Hinchcliffe et al. fabricated tensile probes composed of PLA with natural jute and flax fiber strands. The purpose of the study was to investigate the improvement of additive manufacturing on mechanical properties via pre-stressing of natural fiber reinforcement. They reported for PLA a compressive strength of 66. In another paper, Revati et al. fabricated composites of pennisetum purpureum (PP) and poly(lactide acid) (PLA). The results showed an improvement of the mechanical properties under compression in cartilage tissue regeneration. The value of the compressive strength for PLA was reported of 2 MPa. [151] In the present study, the improvement of the compressive strength for PLA was obtained with a value of 90 MPa (see Figure 5-16).

For nylon 6 there are also a few studies under compression. Chen et al. evaluated the compressive strength of neat nylon 6 through diverse compression rates (CR) and they reported a maximum value of about 110 MPa.[152] The work of Northolt et al. correlated the glass transition temperature with compressive strength for a few materials. They reported a similar value of 90 MPa for neat nylon 6. [153] In another work, Srivastava et al. reported a compressive strength of composites materials comprising of Nylon 6/6 and E-glass fiber. The value attained was of about 60 MPa for neat nylon (53). [154]

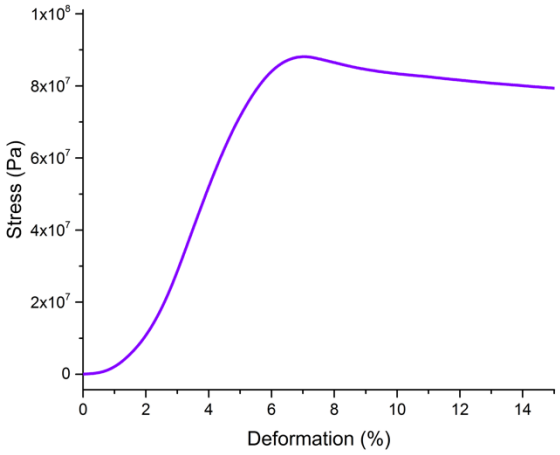

Figure 5-16 Strain-stress curve for $SM_{20}PA_{10}PLA_{70}$ under tension

5.4 Conclusions

The thermal properties showed an increasing T_g for all blends, but that blend with 20 wt % showed better tensile properties $SM_{20}PA_{10}PLA_{70}$. Also this blend showed two melting points in first and second heating at DSC. Two crystallization peaks as well were observed for $SM_{20}PA_{10}PLA_{70}$. A visible thermal degradation was not appreciated in the TGA plots in the range from 0-245 °C. The maximum mass loss was of about 1.6 % belonging only to PA 6, the rest of the blends had 0.3 % of mass loss in the same range.

The mechanical properties were evaluated through tensile and compressive tests. The tensile test showed a strain-stress curve as a brittle material but with enough properties (Young's modulus= 4 GPa and around 30 MPa as maximum stresses). Moreover, the compression test showed a better behavior with a plasticizing strain-stress curve. The yield point attained approximately 60 MPa. This compressive strength can be

compared with that of PEEK and even surpassing the load capacity, because this ternary blend can resist until near of 10 000 N of force.

The higher viscosity showed in the shear-stress curve obtained through linear rheology also supported the possible interactions due to hydrogen bondings. As this testing must be done under a flow fluid pattern PLA, SMMA and PA 6 can be understood as melted totally above 235 °C, and no thermal degradation was observed in the thermogravimetric curves on TGA.

CHAPTER 6. FINITE ELEMENT ANALYSIS OF MODEL WITH LUMBAR FUSION CAGE

6.1 Model with a fusion cage device

Lee at al. [18] reported high stress of about 500 MPa of different fusion cages. These high values are due to the fusion cage placing, which usually is placed on the cancellous bone. A new device has been proposed in this research work with appropriate dimensions to be placed in the center of the intervertebral disc space. To avoid subsidence, the device grasps the cortical bone walls of the vertebra, reducing the subsidence term. The dimensions and shape of the fusion cage are showed in Figure 6-1. The design also has an inner-slot cavity which can facilitate bone fusion. The spaces left by rounded edges allow the bone fusion also in the surroundings of the cage. The extremes of the cage are grasped to the cortical bone to prevent subsidence. Besides this shape is accompanied by the mechanical and rheological properties of the $SM_{20}PA_{10}PLA_{70}$ ternary blend.

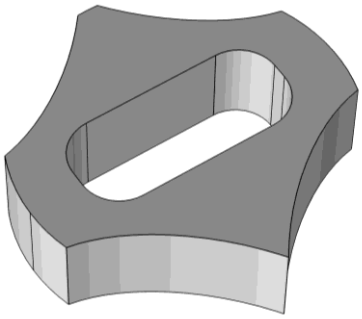

Figure 6-1 Flat intervertebral fusion cage

6.2 Model with fusion device

6.2.1 Flexion moment on model with device

Once the new device was designed, the L2-L3 disc was removed and the fusion device was inserted into the intervertebral disc space. The parameters obtained during tensile and compressive tests were introduced in the simulator.

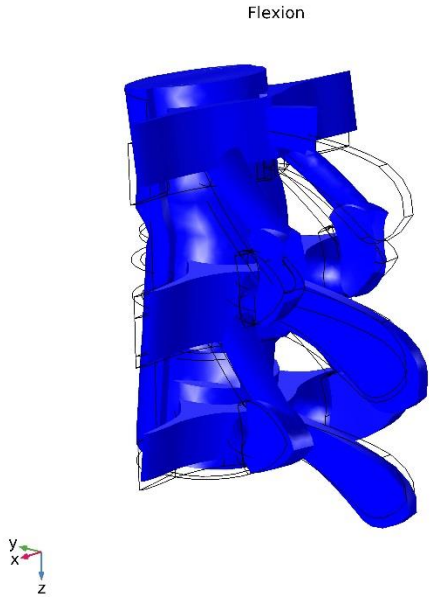

Figure 6-2 Flexion under bending moments on X-axis.

Figure 6-2 displays the motion of the L1-L3 model under flexion moments of 5.85 N-m.

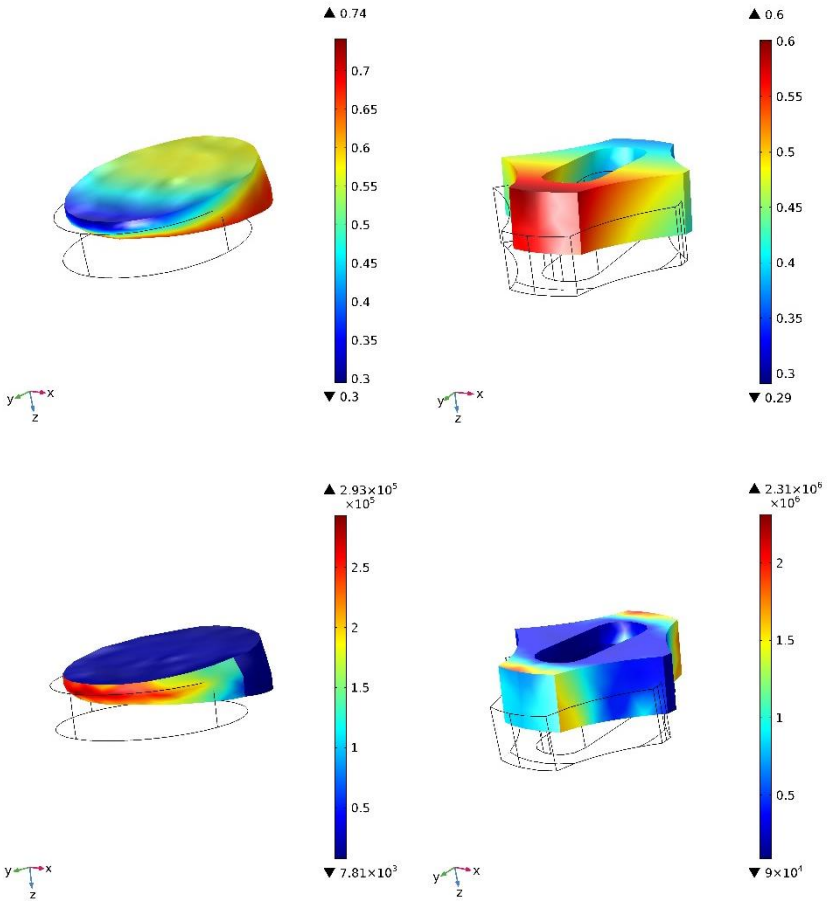

Figure 6-3 Flexion displacements (mm) and von Mises stresses (Pa) in a modified model under bending moments in x direction.Upper left: superior IVD displacement. Upper right: device displacement. Bottom left: superior von Mises stresses. Bottom right: device von Mises stresses.

The displacements of the superior and inferior IVD changed when the device replaced the IVD in the model. The superior IVD showed a maximum displacement of 0.74 mm whereas the device had 0.6 mm. This means the device decreased the displacement value when the device was placed (Figure 6-3). These displacements were similar to those presented by the intact L1-L3 model. Concerning von Mises stresses, the superior IVD had a maximum von Mises stress of about 0.29 MPa and the device experienced 2.31 MPa.

These results agree with the adjacent segment degeneration (ASDeg). This term is defined as the “natural disc deterioration adjacent to the surgically treated disc, without symptoms” [155]. In other words, when a disc is removed partially, or totally the adjacent level can suffer less mobility. This decrease in motion of the intact lumbar section regarding arthrodesis is reported by other researchers in vitro. [156] [157] [158] Also, another author studied the facet joints forces when the intervertebral disc is removed. The forces acting on a removed level increased up to 85 % in comparison to intact.[159]

6.2.2 Lateral moments

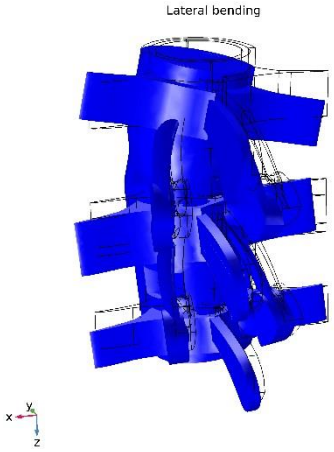

Figure 6-4 Lateral bending of L1-L3 lumbar model

Figure 6-4 shows lateral bending when moments are applied. The highest values found were those present in the pedicles of L1-L2 with values of about 23 MPa as maximum. When comparing these results with the intact model we can observe similar values. The

von Mises in the facet joints were about 2-5 MPa. As mentioned in the intact model these values were closer to what reported Asgharzadeh et al.(2014). [71]

As was expected, the displacements of the model with removed disc had slightly lower values than the intact model (Figure 6-5). In the intact model the superior IVD had 1.97 mm of displacement whereas the inferior IVD had 2.14 mm. The device model presented 1.56 mm of maximum displacement in the superior IVD and the device presented 1.14 mm, with a reduction of total displacement concerning the Level L2-L3 mainly. The von Mises in the intact model were of 0.63 MPa in the superior IVD, whilst the device presented a higher von Mises value of 4.84 MPa.

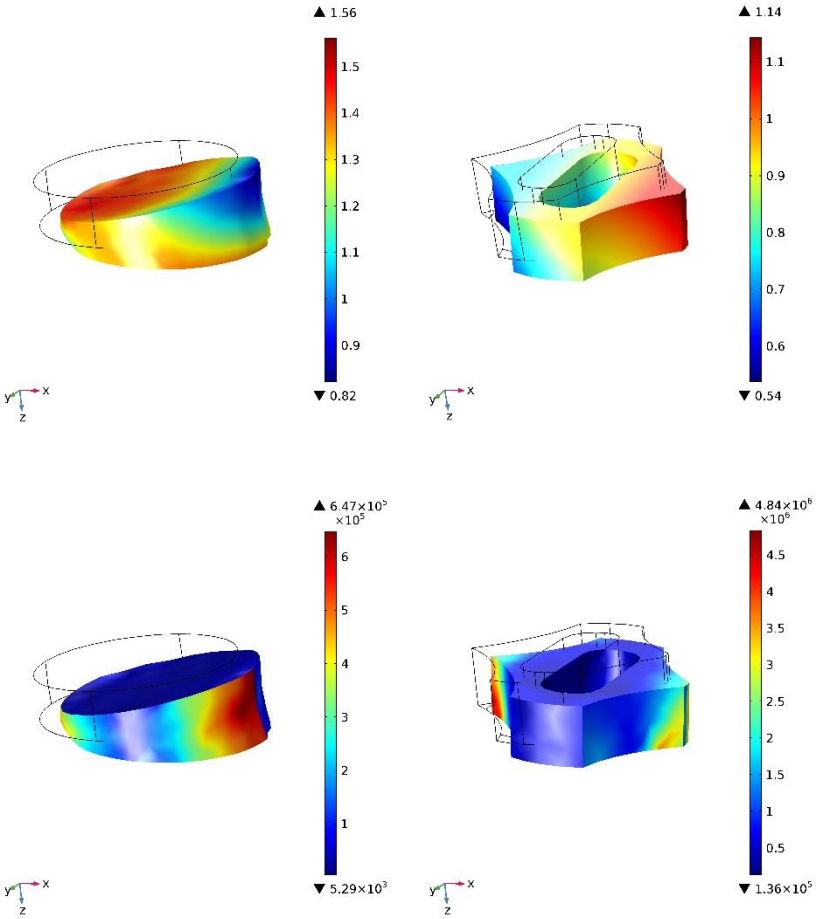

Figure 6-5. Lateral displacements (mm) and von Mises stresses (Pa). upper left: superior IVD displacement, bottom left: inferior IVD von Mises. Upper right: von Mises of superior IVD, bottom right: von Mises stresses of inferior device.

6.2.3 Torsional moment

There was a difference in the intact and device model. The superior IVD showed a maximum displacement of 1.8 mm, a closer value to the intact superior IVD (Figure 6-6). Otherwise, the inferior IVD showed a higher displacement of 2.09 mm, slightly above the intact inferior IVD. The von Mises stresses were higher in the intact model. For example, the superior IVD with a value of 0.85 MPa, a lower value than the model with the device (28 MPa).

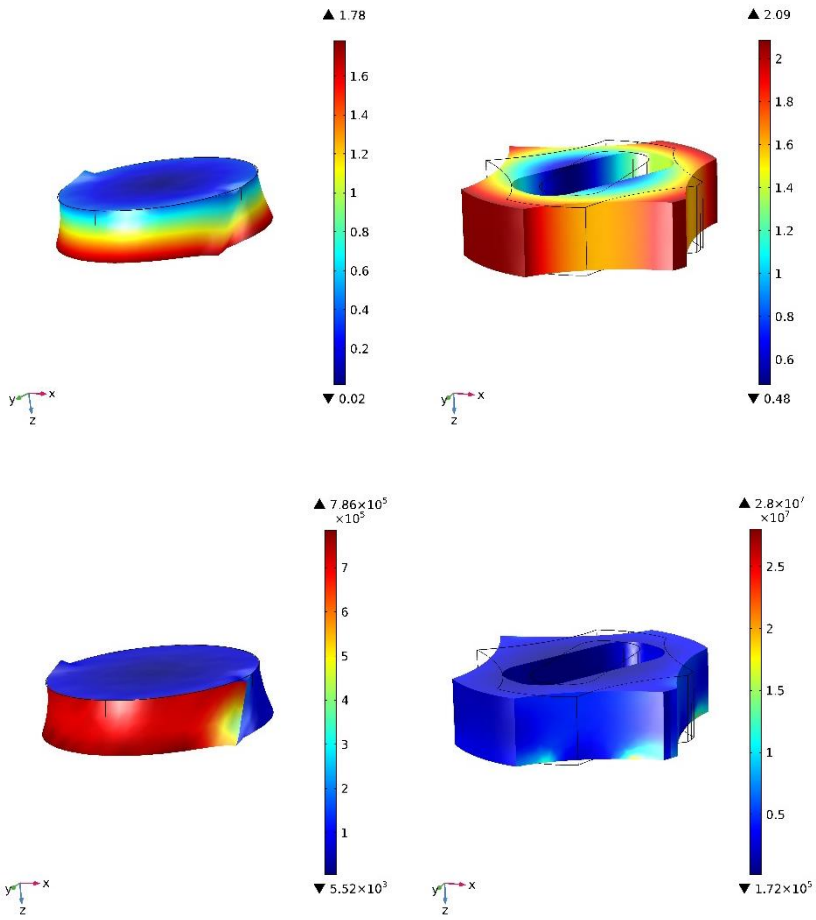

Figure 6-6. Torsional displacements (mm) and von Mises stresses (Pa). Upper left: superior IVD displacement, bottom left: superior IVD von Mises. Upper right: Displacement of device, bottom right: von Mises stresses of inferior device.

6.2.4 Compression

By applying 300 N compressively the superior IVD showed a maximum displacement of 0.77 mm, 0.19 mm less than the intact superior IVD showing a reduction in natural motion. Of the same manner, the inferior IVD was higher in the intact inferior IVD than the device displacement. The device was displaced about 0.007 mm, whereas

the inferior IVD in the intact model presented 0.4 mm of maximum displacement (Figure 6-7).

The von Mises stresses were higher in the intact superior IVD than in the superior IVD with the device included. The device showed 5.18 MPa and the superior IVD had 0.45 MPa as maximum values. The inferior intact IVD showed a maximum von Mises stress of 0.89 MPa, but the device exceeded this value attaining 5.18 MPa.

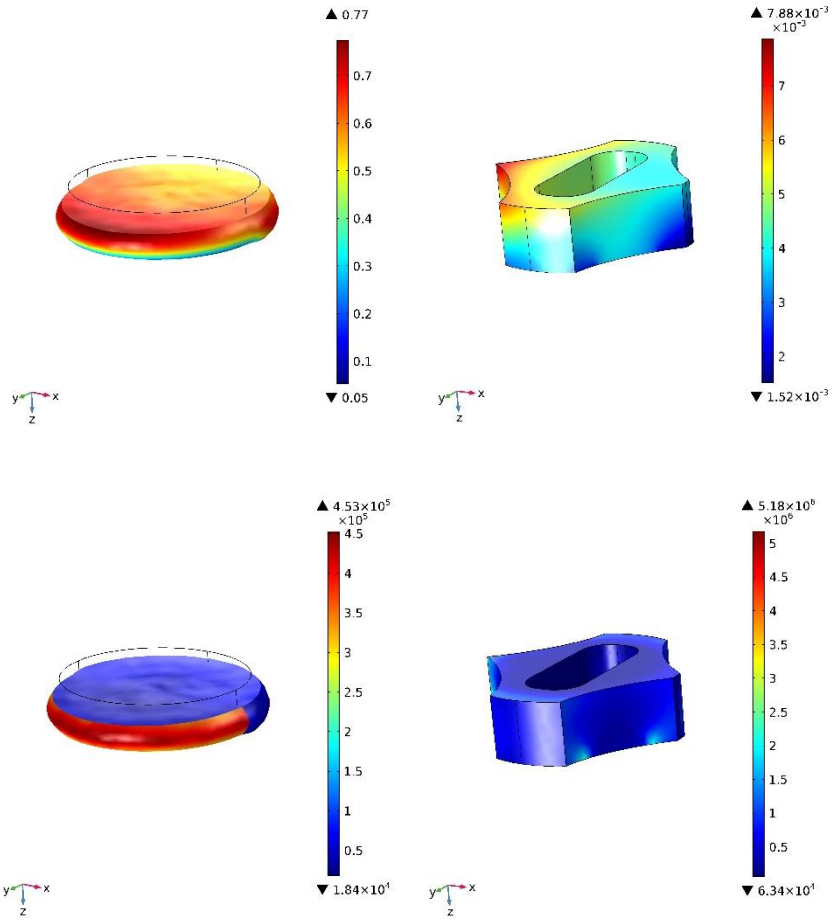

Figure 6-7. Compressive displacements (mm) and von Mises stresse (Pa). Upper left: superior IVD displacement, bottom left: superior IVD von Mises. Upper right: Displacement of device, bottom right: von Mises stresses of inferior device.

The fusion cage mainly functions under compression loads. As we see in the mechanical properties in chapter 7, there is a duality behavior of the ternary polymer blend, being the tensile strength weak when compared with compressive strength. This last resulted in an extraordinary capacity to support a compressive force of about 9000 N without plasticizing. The deformation had a limit of 4.5 (%) in the elastic zone, and the stress yield point was about 70 MPa. These values are enough to ensure no failure under compression of the material according to von Mises theory.

6.3 Conclusions

A few ternary polymer blends were elaborated. Through the evaluation of mechanical properties on the tensile mode, the $SM_{20}PA_{10}PLA_{70}$ blend resulted in best Young's modulus, maximum stress, and elongation at break (%). The evaluation of rheological properties demonstrated a possible duality behavior of the material, and the compression testing was done. An excellent compressive strength resulted. Simultaneously a parallel finite element analysis was conducted. An L1-L3 model was built and it was evaluated under two conditions: 1) without removing intervertebral discs and 2) by replacing the inferior IVD for a new design of fusion cage. Each condition faced four loading types: flexion, lateral, torsional moments, and a compressive force. The results obtained in the finite element analysis were validated with pertinent literature. The von Mises stresses were far from the stresses obtained in the experimental part, which ensure no failure for the device under given loads. This polymeric material represents a potential candidate to compete with more expensive polymers in similar biomedical applications.

CHAPTER 7. GENERAL CONCLUSIONS

Two polymer blends were developed and studied. A binary blend comprised of PLA and SMMA copolymer demonstrated good compatibility due to the improvement of Young's modulus and elongation at break. These polymer blend could produce scaffolds by removing the biodegradable phase (PLA) and leaving the inhert phase belonging to SMMA copolymer, which is very used in bone cement materials. A prototype extruder was built and uniform filaments were produced. The processing conditions don not affect

thermally the blends, presenting a maximum mass loss of 0.3 % at 195 °C. After the filament production, a printing-trail header was built and the filament demonstrated proper viscosity for the 3d printing process. Final pieces were produced by 3d printing.

Second, polymer materials were produced as ternary polymer blends. The melting point of PA 6 did not affect thermally to PLA and SMMA at temperatures of mixing and molding processes. The blend with 10% of PA 6 and 20% of SMMA did show the best tensile properties attaining Young's modulus= 4 GPa and poisson coefficient= 0.38. Maximum stress values were about 30 MPa. The same blend also had excellent compressive strength with Young's modulus=9.6 GPa and poisson coefficient of 0.42. The yield stress was observed at 60 MPa with a load capacity of 10 000 N in the elastic zone. Good interactions of polymers and copolymer were attributed due to the glass transition and melting point temperatures displacements. Similarly, all blends exhibited better viscosity than PLA, which ensures good procesability and thermal resistance. However, the filament production was not reached because the melting point of PA 6, which demands a different extruder prototype or specific modifications.

Similarly, a L1-L3 lumbar model was built through computer aided design (CAD) and two simulations were done: A) intact lumbar model and B) lumbar model with lumbar fusion cage device. About 2 million elements were analyzed under flexion moments of 5.85 Nm, torsional moments= 7.2 Nm and compressive force of 300 N. The results of the intact model allowed to know the maximum von Mises stresses presented in natural components of the model. Those values were validated with specific biomechanical literature. Posteriorly, a lumbar fusion cage was designed with specific characteristics to avoid conflict of interest. The device also has a traditional inner cavity to hold bone, but

the body is wider than other commercial devices with the purpose of being in contact with cortical bone and to avoid subsidence. In the second simulation the inferior intervertebral disc was replaced by the device with material's properties obtained experimentally and were introduced in the software. The results of von Mises stress were also validated with other research works showing that the material can give the needed support under the application. These new kinds of ternary polymer blends can be an option when various properties are sought in implants as partial biodegradability and adequate mechanical properties because traditional polymers can offer sometimes isolated properties.

From the academic point of view, three parallel methodologies were developed in the present thesis. A first dedicated to the study of the polymer science, a second one addressed to addtivie manufacturing, and lastly, a design methodology through finite element analysis. This material can be a good base line to depart to other ternary polymer blends with different applications given the sustainability issues legally worldwide.

REFERENCES

1. Leucht P, Fischer K, Muhr G, Mueller EJ. Epidemiology of traumatic spine fractures. *Injury*. 2009;40(2):166-172. doi:10.1016/j.injury.2008.06.040
2. Heinzelmann M, Wanner GA. Thoracolumbar Spinal Injuries 31. 1980;5(5):463-477. doi:978-3-540-69091-7
3. Martini F, Timmons M, Tallitsch R. The Nervous System: The Spinal Cord and Spinal Nerves. *Hum Anat*. 2012:368-392. doi:10.1023/A:1015257004839

4. Watters WC, Baisden J, Gilbert TJ, et al. Degenerative lumbar spinal stenosis: an evidence-based clinical guideline for the diagnosis and treatment of degenerative lumbar spinal stenosis. *Spine J*. 2008;8(2):305-310. doi:10.1016/j.spinee.2007.10.033
5. Burgstaller JM, Porchet F, Steurer J, Wertli MM. Arguments for the choice of surgical treatments in patients with lumbar spinal stenosis – a systematic appraisal of randomized controlled trials. *BioMed Cent Musculoskelet Disord*. 2015;16(96):1-9. doi:10.1186/s12891-015-0548-8
6. Sobottke R, Siewe J, Kaulhausen T, Otto C, Eysel P. Interspinous Spacers as Treatment for Lumbar Stenosis. *Semin Spine Surg*. 2011;23(1):27-33. doi:10.1053/j.semss.2010.12.002
7. Puzzilli F, Gazzeri R, Galarza M, et al. Interspinous spacer decompression (X-STOP) for lumbar spinal stenosis and degenerative disk disease: a multicenter study with a minimum 3-year follow-up. *Clin Neurol Neurosurg*. 2014;124:166-174. doi:10.1016/j.clineuro.2014.07.004
8. Emary PC. Diagnosis of a 64-year-old patient presenting with suspected lumbar spinal stenosis : an evidence-based case report. 2015;3194(1).
9. Delitto A, Piva SR, Moore CG, et al. Surgery Versus Nonsurgical Treatment of Lumbar Spinal Stenosis. *Ann Intern Med*. 2015;162(7):465. doi:10.7326/M14-1420
10. Poon CS, Doumanian J, Sze G, Johnson MH, Johnson CE, Lin F. Spine and Spinal Canal. In: Reiser, Maximilian F (Institute for Clinical RadiologyLudwig-Maximilian University of Munich, Munich G, Semmler, Wolfhard (Division of Medical Physics in Radiology GCRC, Hedvig, Hricak (Department of Radiology, Memorial Sloan-

Kettering Cancer Center, New York U, eds. *Magnetic Resonance Tomography*. Springer,. Berlin; 2008:535-662. doi:10.1007/978-3-540-29355-2_4

11. Jiang YQ, Che W, Wang HR, Li RY, Li XL, Dong J. Minimum 5 year follow-up of multi-segmental lumbar degenerative disease treated with discectomy and the Wallis interspinous device. *J Clin Neurosci*. 2015;22(7):1144-1149. doi:10.1016/j.jocn.2014.12.016
12. Yoshihara H, Yoneoka D. National trends in the surgical treatment for lumbar degenerative disc disease: United States, 2000 to 2009. *Spine J*. 2015;15(2):265-271. doi:10.1016/j.spinee.2014.09.026
13. Iencean SM. Classification of spinal injuries based on the essential traumatic spinal mechanisms. *Spinal Cord*. 2003;41(7):385-396. doi:10.1038/sj.sc.3101468
14. Heidari P, Pedram H, Zarei MR, et al. Spinal fractures resulting from traumatic injuries. *Chin J Traumatol*. 2010;13(1):3-9. doi:10.3760/cma.j.issn.1008-1275.2010.01.001
15. Phan K, Mobbs RJ. Evolution of Design of Interbody Cages for Anterior Lumbar Interbody Fusion. *Orthop Surg*. 2016;8(3):270-277. doi:10.1111/os.12259
16. AD BJS. A carbon fiber implant to aid interbody lumbar fusion. Two-year clinical results in the first 26 patients. *Spine (Phila Pa 1976)*. 1993;(18):21062117.
17. Fantigrossi A, Galbusera F, Teresa M, Sassi M, Fornari M. Biomechanical analysis of cages for posterior lumbar interbody fusion. 2007;29:101-109. doi:10.1016/j.medengphy.2006.02.007
18. Lee YH, Chung CJ, Wang CW, et al. Computational comparison of three posterior lumbar interbody fusion techniques by using porous titanium interbody cages with

50% porosity. *Comput Biol Med*. 2016;71:35-45. doi:10.1016/j.compbiomed.2016.01.024

19. Hunt J. WO 2010/080511 Al (81). 2010;2010(July).
20. Clavel Escribano M. Fusión intersomática lumbar posterior con jaulas de Brantigan. Estudio inicial. *Neurocirugia*. 1995;6(4):295-300. doi:10.1016/S1130-1473(95)70767-9
21. Jain S, Eltorai AEM, Ruttiman R, Daniels AH. Advances in Spinal Interbody Cages. *Orthop Surg*. 2016;8(3):278-284. doi:10.1111/os.12264
22. Dmuschewsky K. (2015). *WO 2015/188887 A1*. Retrieved from
23. Kleiner JB. (2016) *US 2016/0374825*. Retrieved from https://www.google.co.uk/patents/US20160374825?dq=spinal+fusion+
24. Caratsch, A. (2016) *WO 2016/207798*. Retrieved from https://www.lens.org/images/patent/WO/2016207798/A1/WO_2016_20779
25. Duffield W. (2016). *US 2016/0374831 A1*. Retrieved from https://patents.google.com/patent/US20160374831A1/en
26. Thomas, Dimauro. (2016). *US 2016/0374821 A1*. Retrieved from https://patents.google.com/patent/US20160374821A1/en?oq=US+2016%2f0374821+A1
27. Kurtz SM. *PEEK BIOMATERIALS HANDBOOK*. (ELSEVIER, ed.). USA: WILLIAM ANDREW; 2012.
28. Xin H, Shepherd DET, Dearn KD. PEEK (Polyether-ether-ketone) Based Cervical Total Disc Arthroplasty: Contact Stress and Lubrication Analysis. *Open Biomed Eng J*. 2012;6:73-79.

29. Evans NT, Torstrick FB, Lee CSD, et al. Acta Biomaterialia orthopedic implants. *Acta Biomater*. 2015;13:159-167. doi:10.1016/j.actbio.2014.11.030

30. Arif MF, Kumar S, Varadarajan KM, Cantwell WJ. Performance of biocompatible PEEK processed by fused deposition additive manufacturing. *Mater Des*. 2018;146:249-259. doi:10.1016/j.matdes.2018.03.015

31. Waddon AJ, Hill MJ, Keller A, Blundell DJ. On the crystal texture of linear polyaryls (PEEK, PEK and PPS). *J Mater Sci*. 1987;22:1773-1784. doi:10.1007/BF01132406

32. Monich PR, Henriques B, Novaes de Oliveira AP, Souza JCM, Fredel MC. Mechanical and biological behavior of biomedical PEEK matrix composites: A focused review. *Mater Lett*. 2016;185:593-597. doi:10.1016/j.matlet.2016.09.005

33. Simsiriwong J, Shrestha R, Shamsaei N, Lugo M, Moser RD. Effects of microstructural inclusions on fatigue life of polyether ether ketone (PEEK). *J Mech Behav Biomed Mater*. 2015;51:388-397. doi:10.1016/j.jmbbm.2015.07.020

34. Brockett CL, Carbone S, Fisher J, Jennings LM. PEEK and CFR-PEEK as alternative bearing materials to UHMWPE in a fixed bearing total knee replacement: An experimental wear study. *Wear*. 2017; 374-375:86-91 . doi:10.1016/j.wear.2016.12.010

35. Niinomi M. Biologically and Mechanically Biocompatible Titanium Alloys. 2008;49(10):2170-2178. doi:10.2320/matertrans.L-MRA2008828

36. Lee JH, Kong C-B, Yang JJ, et al. Comparison of fusion rate and clinical results between CaO-SiO2-P2O5-B2O3 bioactive glass ceramics spacer with titanium cages in posterior lumbar interbody fusion. *Spine J*. 2016;16:1367-1376. doi:10.1016/j.spinee.2016.07.531

37. Norouzi E, Atapour M, Shamanian M, Allafchian A. Effect of bonding time on the joint properties properties of transient liquid phase bonding between Ti-6Al-4V and AISI 304 . *Mater Des*. 2017;701:335-341. doi:10.1016/j.matdes.2016.03.101

38. Colic K, Sedmak A, Gubeljak N, Burzic M, Hut I. 3D Experimental optical analysis of titanium alloys for biomedical applications. In: *INES 2011 - 15th International Conference on Intelligent Engineering Systems, Proceedings*. 2011;399-403. doi:10.1109/INES.2011.5954780

39. Crisan N, Trunfio-Sfarghiu A-M, Gordin D, Gheorghiu H, Stoica G, Berthier Y. A new titanium alloy for biomedical applications. *2011 E-Health Bioeng Conf*. 2011;1-4

40. X. Tian, C. Gong, S. Yang, Z. Luo, R.K.Y. Fu, P.K. Chu, Oxygen plasma ion implantation of biomedical titanium alloy, IEEE Trans. Plasma Sci. 2006;34: 1235–1240. doi:10.1109/TPS.2006.879002.

41. Hodgskinson R, Currey JD, Evans GP. Hardness, an indicator of the mechanical competence of cancellous bone. *J Orthop Res*. 1989;7(5):754-758. doi:10.1002/jor.1100070518

42. Todoh M, Ihara M, Matsumoto T, Tanaka M. Relationship between Mechanical Property of Cancellous Bone and Hardness of Trabeculae. *JSME Int J Ser C*. 2004;47(4):1075-1078. doi:10.1299/jsmec.47.1075

43. Wang Q, Liu Z, Yang D, Mohsan AUH. Metallurgical-based prediction of stress-temperature induced rapid heating and cooling phase transformations for high speed machining Ti-6Al-4V alloy. *Mater Des*. 2017;119:208-218. doi:10.1016/j.matdes.2017.01.076

44. Fortney A, Fossum E. Soluble, semi-crystalline PEEK analogs based on 3,5-difluorobenzophenone: Synthesis and characterization. *Polymer*. 2012;53:2327-2333. doi:10.1016/j.polymer.2012.03.056

45. R. Pederson, Microstructure and Phase Transformation of Ti-6Al-4V, Lulea University of Technology, 2002.

46. Larson AN, Baky FJ, St Hilaire T, et al. Spine Deformity With Fused Ribs Treated With Proximal Rib- Versus Spine-Based Growing Constructs. *Spine Deform*. 2019;7(1):152-157. doi:10.1016/j.jspd.2018.05.011

47. Wang H, Chen W, Jiang J, Lu F, Ma X, Xia X. Analysis of the correlative factors in the selection of interbody fusion cage height in transforaminal lumbar interbody fusion. *BMC Musculoskelet Disord*. 2016;17(9). doi:10.1186/s12891-016-0866-5

48. Hodgskinson R, Currey JD. Young's modulus, density and material properties in cancellous bone over a large density range. *J Mater Sci Mater Med*. 1992;3:377-381. doi:10.1007/BF00705371

49. Totoribe K, Tajima N, Chosa E. A biomechanical study of posterolateral lumbar fusion using a three-dimensional nonlinear finite element method. *J Orthop Sci*. 1999;4:115-126.

50. Ding M, Danielsen CC, Hvid I, Overgaard S. Three-dimensional microarchitecture of adolescent cancellous bone. *Bone*. 2012;51:953-960. doi:10.1016/j.bone.2012.07.018

51. Jiang R, Kleer R, Piller FT. Predicting the future of additive manufacturing: A Delphi study on economic and societal implications of 3D printing for 2030. *Technol Forecast Soc Change*. 2017;117:84-97. doi:10.1016/j.techfore.2017.01.006

52. Berretta S, Evans K, Ghita O. Additive manufacture of PEEK cranial implants: Manufacturing considerations versus accuracy and mechanical performance. *Mater Des*. 2018;139:141-152. doi:10.1016/j.matdes.2017.10.078

53. Bartolomeu F, Abreu CS, Moura CG, et al. Ti6Al4V-PEEK multi-material structures – design, fabrication and tribological characterization focused on orthopedic implants. *Tribol Int*. 2019;131:672-678. doi:10.1016/j.triboint.2018.11.017

54. Burton HE, Peel S, Eggbeer D. Reporting fidelity in the literature for computer aided design and additive manufacture of implants and guides. *Addit Manuf*. 2018;23:362-373. doi:10.1016/j.addma.2018.08.027

55. Gómez-Olivencia A, Arlegi M, Barash A, Stock JT, Been E. The Neandertal vertebral column 2: The lumbar spine. *J Hum Evol*. 2017;106:84-101. doi:10.1016/j.jhevol.2017.01.006

56. Dreischarf M, Rohlmann A, Bergmann G, Zander T. Optimised in vitro applicable loads for the simulation of lateral bending in the lumbar spine. *Med Eng Phys*. 2012;34(6):777-780. doi:10.1016/j.medengphy.2012.04.002

57. Kim H-J, Chun H-J, Lee H-M, et al. The biomechanical influence of the facet joint orientation and the facet tropism in the lumbar spine. *Spine J*. 2013;13(10):1301-1308. doi:10.1016/j.spinee.2013.06.025

58. Goel VK, Mehta A, Jangra J, et al. Anatomic Facet Replacement System (AFRS) Restoration of Lumbar Segment Mechanics to Intact: A Finite Element Study and In Vitro Cadaver Investigation. *SAS J*. 2007;1(1):46-54. doi:10.1016/S1935-9810(07)70046-4

59. Dreischarf M, Zander T, Shirazi-Adl A, et al. Comparison of eight published static

finite element models of the intact lumbar spine: Predictive power of models improves when combined together. *J Biomech*. 2014;47(8):1757-1766. doi:10.1016/j.jbiomech.2014.04.002

60. García Vacas F, Ezquerro Juanco F, Pérez De La Blanca A, Prado Novoa M, Postigo Pozo S. The flexion-extension response of a novel lumbar intervertebral disc prosthesis: A finite element study. *Mech Mach Theory*. 2014;73:273-284. doi:10.1016/j.mechmachtheory.2013.11.013
61. Noone G, Mazumdar J, Ghista DN, Tansley GD. Asymmetrical loads and lateral bending of the human spine. *Med Biol Eng Comput*. 1993;31(1):131-136. doi:10.1007/BF02446661
62. Kupper T, Haisch M. Lumbar spine loads during education and training with self-contained breathing apparatus. *Int Arch Occup Environ Health*. 2000;73(1):35-40. http://www.ncbi.nlm.nih.gov/pubmed/10672489.
63. Oxland TR. Fundamental Biomechanics of the Spine-What we have learned in the past 25 years and future directions. *J Biomech*. 2016(49);6:817-832. doi:10.1016/j.jbiomech.2015.10.035
64. Pitzen T, Geisler FH, Matthis D, Müller-Storz H, Pedersen K, Steudel WI. The influence of cancellous bone density on load sharing in human lumbar spine: A comparison between an intact and a surgically altered motion segment. *Eur Spine J*. 2001;10(1):23-29. doi:10.1007/s005860000223
65. Kamińska J, Roman-Liu D, Zagrajek T, Borkowski P. Differences in lumbar spine load due to posture and upper limb external load. *Int J Occup Saf Ergon*. 2010;16(4):421-430. doi:10.1080/10803548.2010.11076857

66. Dreischarf M, Shirazi-Adl A, Arjmand N, Rohlmann A, Schmidt H. Estimation of loads on human lumbar spine: A review of in vivo and computational model studies. *J Biomech*. 2016;49(6):833-845. doi:10.1016/j.jbiomech.2015.12.038

67. Wettenschwiler PD, Lorenzetti S, Ferguson SJ, et al. Loading of the lumbar spine during backpack carriage. *Comput Methods Biomech Biomed Engin*. 2017(20);5:558-565. doi:10.1080/10255842.2016.1261849

68. Bouzakis KD, Mitsi S, Michailidis N, et al. Loading simulation of lumbar spine vertebrae during a compression test using the finite elements method and trabecular bone strength properties, determined by means of nanoindentations. *J Musculoskelet Neuronal Interact*. 2004;4(2):152-158.

69. Newell N, Little JP, Christou A, Adams MA, Adam CJ, Masouros SD. Biomechanics of the human intervertebral disc: A review of testing techniques and results. *J Mech Behav Biomed Mater*. 2017;69:420-434. doi:10.1016/j.jmbbm.2017.01.037

70. Marini G, Huber G, Püschel K, Ferguson SJ. Nonlinear dynamics of the human lumbar intervertebral disc. *J Biomech*. 2015;48:479-498. doi:10.1016/j.jbiomech.2014.12.006

71. Asgharzadeh Shirazi H, Ayatollahi MR. Biomechanical analysis of functionally graded biomaterial disc in terms of motion and stress distribution in lumbar spine. *Int J Eng Sci*. 2014;84:62-78. doi:10.1016/j.ijengsci.2014.06.008

72. Byrne RM, Zhou Y, Zheng L, Chowdhury SK, Aiyangar A, Zhang X. Segmental variations in facet joint translations during in vivo lumbar extension. *J Biomech*. 2017;70:88-95. doi:10.1016/j.jbiomech.2017.09.026

73. Cochran T. (2017) *EP 3 068 834 B1. Retrieved from*

https://patents.google.com/patent/EP3068834A1/un

74. Chuai CZ, Almdal K, Lyngaae-jørgensen J. Phase continuity and inversion in polystyrene / poly (methyl methacrylate) blends. 2003;44:481-493.

75. Bouzid L, Hiadsi S, Bensaid MO, Foudad FZ. Molecular dynamics simulation studies of the miscibility and thermal properties of PMMA/PS polymer blend. *Chinese J Phys*. 2018;56(6):3012-3019. doi:10.1016/j.cjph.2018.09.034

76. Tüzüner Ş, Demir MM. Dispersion of organophilic Ag nanoparticles in PS-PMMA blends. *Mater Chem Phys*. 2015;162:692-699. doi:10.1016/j.matchemphys.2015.06.044

77. Yun M, Jung N, Yim C, Jeon S. Nanomechanical thermal analysis of the effects of physical aging on glass transitions in PS/PMMA blend and PS-PMMA diblock copolymers. *Polymer (Guildf)*. 2011;52(18):4136-4140. doi:10.1016/j.polymer.2011.06.051

78. Nofar M, Sacligil D, Carreau PJ, Kamal MR, Heuzey M-C. Poly (lactic acid) blends: Processing, properties and applications. *Int J Biol Macromol*. 2018;125:307-360. doi:10.1016/j.ijbiomac.2018.12.002

79. Narayanan G, Vernekar VN, Kuyinu EL, Laurencin CT. Poly (lactic acid)-based biomaterials for orthopaedic regenerative engineering. *Adv Drug Deliv Rev*. 2016;107:247-276. doi:10.1016/j.addr.2016.04.015

80. Pucci JU, Christophe BR, Sisti J a., Connolly ES. Three-dimensional printing: technologies, applications, and limitations in neurosurgery. *Biotechnol Adv*. 2017;35(5):521-529. doi:10.1016/j.biotechadv.2017.05.007

81. Henkel J, Woodruff MA, Epari DR, et al. Bone Regeneration Based on Tissue

Engineering Conceptions – A 21st Century Perspective. *Nat Publ Gr*. 2013;1(3):216-248. doi:10.4248/BR201303002

82. Bodaghi M, Damanpack a. R, Hu GF, Liao WH. Large deformations of soft metamaterials fabricated by 3D printing. *Mater Des*. 2017;131:81-91. doi:10.1016/j.matdes.2017.06.002

83. Chacón JM, Caminero M a., García-Plaza E, Núñez PJ. Additive manufacturing of PLA structures using fused deposition modelling: Effect of process parameters on mechanical properties and their optimal selection. *Mater Des*. 2017;124:143-157. doi:10.1016/j.matdes.2017.03.065

84. An J, Teoh JEM, Suntornnond R, Chua CK. Design and 3D Printing of Scaffolds and Tissues. *Engineering*. 2015;1(2):261-268. doi:10.15302/J-ENG-2015061

85. Senatov FS, Niaza K V, Zadorozhnyy MY, Maksimkin a. V, Kaloshkin SD, Estrin YZ. Mechanical properties and shape memory effect of 3D-printed PLA-based porous scaffolds. *J Mech Behav Biomed Mater*. 2016;57:139-148. doi:10.1016/j.jmbbm.2015.11.036

86. Kaur M, Yun TG, Han SM, Thomas EL, Kim WS. 3D printed stretching-dominated micro-trusses. *Mater Des*. 2017;134:272-280. doi:10.1016/j.matdes.2017.08.061

87. Farah S, Anderson DG, Langer R. Physical and mechanical properties of PLA, and their functions in widespread applications - A comprehensive review. *Adv Drug Deliv Rev*. 2016;107:367-392. doi:10.1016/j.addr.2016.06.012

88. Russias J, Saiz E, Nalla RK, Gryn K, Ritchie RO, a.P. Tomsia. Fabrication and mechanical properties of PLA/HA composites: A study of in vitro degradation. *Mater Sci Eng C*. 2006;26(8):1289-1295. doi:10.1016/j.msec.2005.08.004

89. Heidari BS, Oliaei E, Shayesteh H, et al. Simulation of mechanical behavior and optimization of simulated injection molding process for PLA based antibacterial composite and nanocomposite bone screws using central composite design. *J Mech Behav Biomed Mater*. 2017;65:160-176. doi:10.1016/j.jmbbm.2016.08.008

90. Michael FM, Khalid M, Walvekar R, et al. Effect of nanofillers on the physico-mechanical properties of load bearing bone implants. *Mater Sci Eng C*. 2016;67:792-806. doi:10.1016/j.msec.2016.05.037

91. Balk M, Behl M, Wischke C, Zotzmann J, Lendlein A. Recent advances in degradable lactide-based shape-memory polymers ☆. *Adv Drug Deliv Rev*. 2016;107:136-152. doi:10.1016/j.addr.2016.05.012

92. Hao X, Kaschta J, Pan Y, Liu X, Schubert DW. Intermolecular cooperativity and entanglement network in a miscible PLA / PMMA blend in the presence of nanosilica. *Polymer (Guildf)*. 2016;82:57-65. doi:10.1016/j.polymer.2015.11.029

93. Middleton JC, Tipton a J. Synthetic biodegradable polymers as orthopedic devices. *Biomaterials*. 2000;21(23):2335-2346. doi:10.1016/S0142-9612(00)00101-0

94. He Z, Zhai Q, Hu M, et al. Bone cements for percutaneous vertebroplasty and balloon kyphoplasty: Current status and future developments. *J Orthop Transl*. 2015;3(1):1-11. doi:10.1016/j.jot.2014.11.002

95. Renganathan. K, PolymerThermodynamics Blends, Copolymers and Reversible Polymerization, 1st ed., Taylor & Francis, 2011. doi:10.1201/b11198-15.

96. Montana JS, Roland S, Richaud E, Miquelard-Garnier G. Nanostructuration effect on the mechanical properties of PMMA toughened by a triblock acrylate copolymer using multilayer coextrusion. *Polymer*. 2018;149:124-133.

doi:10.1016/j.polymer.2018.06.048

97. Nofar M, Tabatabaei a., Sojoudiasli H, et al. Mechanical and bead foaming behavior of PLA-PBAT and PLA-PBSA blends with different morphologies. *Eur Polym J*. 2017;90(February):231-244. doi:10.1016/j.eurpolymj.2017.03.031
98. Canetti M, Cacciamani A, Bertini F. Miscible blends of polylactide and poly(methyl methacrylate): Morphology, structure, and thermal behavior. *J Polym Sci Part B Polym Phys*. 2014;52(17):1168-1177. doi:10.1002/polb.23544
99. Gere D, Czigany T. Rheological and mechanical properties of recycled polyethylene films contaminated by biopolymer. *Waste Manag*. 2018;76:190-198. doi:10.1016/j.wasman.2018.02.045
100. Hamad K, Kaseem M, Deri F, Ko YG. Mechanical properties and compatibility of polylactic acid/polystyrene polymer blend. *Mater Lett*. 2016;164:409-412. doi:10.1016/j.matlet.2015.11.029
101. Li K, Huang J, Xu D, Zhong Y, Zhang L, Cai J. Mechanically strong polystyrene nanocomposites by peroxide-induced grafting of styrene monomers within nanoporous cellulose gels. *Carbohydr Polym*. 2018;199:473-481. doi:10.1016/j.carbpol.2018.07.034
102. Li R, Yu W, Zhou C. Mechanically strong polystyrene nanocomposites by peroxide-induced grafting of styrene monomers within nanoporous cellulose gels. 2018;199:473-481. doi:10.1007/s00289-005-0499-6
103. Huang Y, Jiang S, Li G, Chen D. Effect of fillers on the phase stability of binary polymer blends: A dynamic shear rheology study. 2005(59);19:51175124. doi:10.1016/j.actamat.2005.07.021

104. Chopra *, § , Marianna Kontop D, Vlassopoulos D, Hatzikiriakos SG. Effect of maleic anhydride content on the rheology and phase behavior of poly(styrene-co -maleic anhydride)/ poly(methyl methacrylate) blends. *Rheol Acta*. 2003;41(1-2):10-24. doi:10.1007/s003970200001

105. Mohammadi M, Yousefi AA, Ehsani M. Thermorheological analysis of blend of high- and low-density polyethylenes. *J Polym Res*. 2012;19(2):24-29. doi:10.1007/s10965-011-9798-9

106. Ding Y, Feng W, Huang D, Lu B, Wang P, Wang G. Compatibilization of immiscible PLA-based biodegradable polymer blends using amphiphilic di-block copolymers. 2019;118:45-52. doi:10.1016/j.eurpolymj.2019.05.036

107. Singla RK, Zafar MT, Maiti SN, Ghosh AK. Physical blends of PLA with high vinyl acetate containing EVA and their rheological, thermo-mechanical and morphological responses. *Polym Test*. 2017;63:398-406. doi:10.1016/j.polymertesting.2017.08.042

108. Maroufkhani M, Katbab AA, Liu W, Zhang J. Polylactide (PLA) and acrylonitrile butadiene rubber (NBR) blends: The effect of ACN content on morphology, compatibility and mechanical properties. *Polymer*. 2017;115:37-44. doi:10.1016/j.polymer.2017.03.025

109. Adrar S, Habi A, Ajji A, Grohens Y. Synergistic effects in epoxy functionalized graphene and modified organo-montmorillonite PLA/PBAT blends. *Appl Clay Sci*. 2018;157:65-75. doi:10.1016/j.clay.2018.02.028

110. Nasti G, Gentile G, Cerruti P, Carfagna C, Ambrogi V. Double percolation of multiwalled carbon nanotubes in polystyrene/polylactic acid blends. *Polymer*

(Guildf). 2016;99:193-203. doi:10.1016/j.polymer.2016.06.058

111. Zhang C, Liu X, Liu H, Wang Y, Guo Z, Liu C. Multi-walled carbon nanotube in a miscible PEO/PMMA blend: Thermal and rheological behavior. *Polym Test*. 2019;75:367-372. doi:10.1016/j.polymertesting.2019.03.003
112. Chiu FC, Yeh SC. Comparison of PVDF/MWNT, PMMA/MWNT, and PVDF/PMMA/MWNT nanocomposites: MWNT dispersibility and thermal and rheological properties. *Polym Test*. 2015;45:114-123. doi:10.1016/j.polymertesting.2015.05.011
113. Mao Z, Zhang X, Jiang G, Zhang J. Fabricating sea-island structure and co-continuous structure in PMMA/ASA and PMMA/CPE blends: Correlation between impact property and phase morphology. *Polym Test*. 2019;73:21-30. doi:10.1016/j.polymertesting.2018.11.008
114. Suresh SS, Mohanty S, Nayak SK. Effect of nitrile rubber on mechanical, thermal, rheological and flammability properties of recycled blend. *Process Saf Environ Prot*. 2019;123:370-378. doi:10.1016/j.psep.2019.01.025
115. Prado BR, Bartoli JR. Synthesis and characterization of PMMA and organic modified montmorilonites nanocomposites via in situ polymerization assisted by sonication. *Appl Clay Sci*. 2018;160:132-143. doi:10.1016/j.clay.2018.02.035
116. Potanin A. Rheology of silica dispersions stabilized by polymers. *Colloids Surfaces A Physicochem Eng Asp*. 2019;562(November 2018):54-60. doi:10.1016/j.colsurfa.2018.11.020
117. Zhang Q, Wu C, Song Y, Zheng Q. Rheology of fumed silica/polypropylene glycol dispersions. *Polymer (Guildf)*. 2018;148:400-406.

doi:10.1016/j.polymer.2018.06.051

118. Zhang G, Zhang J, Shenguo W, Shen D. Miscibility and phase structure of binary blends of polylactide and poly(methyl methacrylate). *J Polym Sci Part B*. 2003;41(4):23-30. doi:10.1002/app.11735

119. Mallick S, Ahmad Z, Touati F, Bhadra J, Shakoor RA, Al-Thani NJ. PLA-TiO2nanocomposites: Thermal, morphological, structural, and humidity sensing properties. *Ceram Int*. 2018;44(14):16507-16513. doi:10.1016/j.ceramint.2018.06.068

120. Yu S, Xiang H, Zhou J, Zhu M. Enhanced flame-retardant performance of poly (lactic acid) (PLA) composite by using intrinsically phosphorus-containing PLA. *Prog Nat Sci Mater Int*. 2018;28(5):590-597. doi:10.1016/j.pnsc.2018.09.002

121. León-Cabezas MA, Martínez-García A, Varela-Gandía FJ. Innovative functionalized monofilaments for 3D printing using fused deposition modeling for the toy industry. *Procedia Manuf*. 2017;13:738-745. doi:10.1016/j.promfg.2017.09.130

122. Tian X, Liu T, Yang C, Wang Q, Li D. Interface and performance of 3D printed continuous carbon fiber reinforced PLA composites. *Compos Part A Appl Sci Manuf*. 2016;88:198-205. doi:10.1016/j.compositesa.2016.05.032

123. Fortelný I, Jůza J. Analysis of the effect of block copolymers on interfacial tension in immiscible polymer blends. *Polymer (Guildf)*. 2018;150:380-390. doi:10.1016/j.polymer.2018.07.041

124. La Mantia FP, Morreale M, Botta L, Mistretta MC, Ceraulo M, Scaffaro R. Degradation of polymer blends: A brief review. *Polym Degrad Stab*. 2017;145:79-

92. doi:10.1016/j.polymdegradstab.2017.07.011

125. Sangroniz A, Gonzalez A, Martin L, Irusta L, Iriarte M, Etxeberria A. Miscibility and degradation of polymer blends based on biodegradable poly(butylene adipate-co-terephthalate). *Polym Degrad Stab*. 2018;151:25-35. doi:10.1016/j.polymdegradstab.2018.01.023

126. Saini P, Arora M, Kumar MNVR. Poly (lactic acid) blends in biomedical applications ☆. *Adv Drug Deliv Rev*. 2016;107:47-59. doi:10.1016/j.addr.2016.06.014

127. Dong W, Zou B, Yan Y, Ma P, Chen M. Effect of chain-extenders on the properties and hydrolytic degradation behavior of the poly(lactide)/ poly(butylene adipate-co-terephthalate) blends. *Int J Mol Sci*. 2013;14(10):20189-20203. doi:10.3390/ijms141020189

128. Hui D, Goodridge RD, Scotchford C a., Grant DM. Laser sintering of nano-hydroxyapatite coated polyamide 12 powders. *Addit Manuf*. 2018;22:560-570. doi:10.1016/j.addma.2018.05.045

129. Yamano N, Kawasaki N, Ida S, Nakayama Y, Nakayama A. Biodegradation of polyamide 4 in vivo. *Polym Degrad Stab*. 2017;137:281-288. doi:10.1016/j.polymdegradstab.2017.02.004

130. Shrestha BK, Mousa HM, Tiwari AP, Ko SW, Park CH, Kim CS. Development of polyamide-6,6/chitosan electrospun hybrid nanofibrous scaffolds for tissue engineering application. *Carbohydr Polym*. 2016;148:107-114. doi:10.1016/j.carbpol.2016.03.094

131. Cossement D, Gouttebaron R, Cornet V, Viville P, Hecq M, Lazzaroni R. PLA-PMMA blends : A study by XPS and ToF-SIMS. 2006;252:6636-6639.

doi:10.1016/j.apsusc.2006.02.225

132. Velasco D, Benito L, Fernández-gutiérrez M, Román JS, Elvira C. The Journal of Supercritical Fluids Preparation in supercritical CO $_2$ of porous poly (methyl methacrylate)– poly (L -lactic acid) (PMMA – PLA) scaffolds incorporating ibuprofen. *J Supercrit Fluids*. 2010;54(3):335-341. doi:10.1016/j.supflu.2010.05.012

133. Wu C, Wang C, Chen C. Influence of asymmetric ratio of polystyrene-block-poly (methyl methacrylate) block copolymer on the crystallization rate of PLA. *Eur Polym J*. 2015;66:160-169. doi:10.1016/j.eurpolymj.2015.02.018

134. Picard E, Vermogen a., Gérard JF, Espuche E. Barrier properties of nylon 6-montmorillonite nanocomposite membranes prepared by melt blending: Influence of the clay content and dispersion state. Consequences on modelling. *J Memb Sci*. 2007;292(1-2):133-144. doi:10.1016/j.memsci.2007.01.030

135. Zhang W, Tang RC. Adsorption and flame retardant properties of potassium diphenyl sulfonate on nylon 6 fabric. *React Funct Polym*. 2018;126:36-43. doi:10.1016/j.reactfunctpolym.2018.03.005

136. He W, Zhu H, Xiang Y, Long L, Qin S, Yu J. Enhancement of flame retardancy and mechanical properties of polyamide 6 by incorporating an aluminum salt of diisobutylphosphinic combined with organoclay. *Polym Degrad Stab*. 2017;144:442-453. doi:10.1016/j.polymdegradstab.2017.09.003

137. Zhou Y, Lei L, Yang B, Li J, Ren J. Preparation and characterization of polylactic acid (PLA) carbon nanotube nanocomposites. *Polym Test*. 2018;68:34-38. doi:10.1016/j.polymertesting.2018.03.044

138. Xu M, Choi YS, Kim YK, Wang KH, Chung IJ. Synthesis and characterization of exfoliated poly(styrene-co-methyl methacrylate)/clay nanocomposites via emulsion polymerization with AMPS. *Polymer (Guildf)*. 2003;44(20):6387-6395. doi:10.1016/S0032-3861(03)00653-0

139. Chen N, Yao X, Zheng C, et al. Study on the miscibility, crystallization and crystalline morphology of polyamide-6/polyvinylidene fluoride blends. *Polymer (Guildf)*. 2017;124:30-40. doi:10.1016/j.polymer.2017.07.040

140. Furushima Y, Schick C, Toda A. Crystallization, recrystallization, and melting of polymer crystals on heating and cooling examined with fast scanning calorimetry. *Polym Cryst*. 2018;1:e10005. doi:10.1002/pcr2.10005

141. Medellín-Rodríguez FJ, Larios-López L, Zapata-Espinoza A, Dávalos-Montoya O, Phillips PJ, Lin JS. Melting Behavior of Polymorphics: Molecular Weight Dependence and Steplike Mechanisms in Nylon-6. *Macromolecules*. 2004;37(5):1799-1809. doi:10.1021/ma030466c

142. Tohidi SD, Rocha AM, Dencheva N V, Denchev Z. Single polymer laminate composites by compression molding of knitted textiles and microparticles of polyamide 6: Preparation and structure-properties relationship. *Compos Part A Appl Sci Manuf*. 2018;109:171-183. doi:10.1016/j.compositesa.2018.03.003

143. Scaffaro R, Lopresti F, Botta L. PLA based biocomposites reinforced with Posidonia oceanica leaves. *Compos Part B Eng*. 2018;139:1-11. doi:10.1016/j.compositesb.2017.11.048

144. Tiwary P, Park CB, Kontopoulou M. Transition from microcellular to nanocellular PLA foams by controlling viscosity, branching and crystallization. *Eur Polym J*.

2017;91:283-296. doi:10.1016/j.eurpolymj.2017.04.010

145. Zhu R, Yadama V, Liu H, Lin RJT, Harper DP. Fabrication and characterization of Nylon 6/cellulose nanofibrils melt-spun nanocomposite filaments. *Compos Part A Appl Sci Manuf*. 2017;97:111-119. doi:10.1016/j.compositesa.2017.02.025

146. Ogunsona EO, Misra M, Mohanty AK. Impact of interfacial adhesion on the microstructure and property variations of biocarbons reinforced nylon 6 biocomposites. *Compos Part A Appl Sci Manuf*. 2017;98:32-44. doi:10.1016/j.compositesa.2017.03.011

147. Coreño-Alonso J, Méndez-Bautista MT. Relación estructura-propiedades de polímeros. *Educ Quim*. 2010;21(4):291-299. doi:10.1016/S0187-893X(18)30098-3

148. Murariu M, Dubois P. PLA composites: From production to properties. *Adv Drug Deliv Rev*. 2016;107:17-46. doi:10.1016/j.addr.2016.04.003

149. Yamaoka I. Toughened polymer blends composed of a ductile styrene-butadiene-styrene matrix with brittle methyl methacrylate-styrene particles. *Polymer (Guildf)*. 1995;36(17):3359-3368. doi:10.1016/0032-3861(95)99437-Y

150. Zanjanijam AR, Hakim S, Azizi H. Rheological, mechanical and thermal properties of the PA/PVB blends and their nanocomposites: Structure-property relationships. *Polym Test*. 2018;66:48-63. doi:10.1016/j.polymertesting.2018.01.006

151. Revati R, Majid MSA, Ridzuan MJM, et al. In vitro degradation of a 3D porous Pennisetum purpureum/PLA biocomposite scaffold. *J Mech Behav Biomed Mater*. 2017;74:383-391. doi:10.1016/j.jmbbm.2017.06.035

152. Chen X, Galeski A, Michler GH. Morphological alteration and strength of polyamide 6 subjected to high plane-strain compression. *Polymer (Guildf)*. 2006;47(9):3171-

3185. doi:10.1016/j.polymer.2006.02.061

153. Northolt MG. Compressive strength and glass transition temperature. *J Mater Sci*. 1981;16(7):2025-2028. doi:10.1007/BF00540658

154. Srivastava VK, Lal S. Mechanical properties of E-glass fibre reinforced nylon 6/6 resin composites. *J Mater Sci*. 1991;26(24):6693-6698. doi:10.1007/BF02402662

155. Charles Malveaux WMS, Sharan AD. Adjacent segment disease after lumbar spinal fusion: A systematic review of the current literature. *Semin Spine Surg*. 2011;23(4):266-274. doi:10.1053/j.semss.2011.05.008

156. Kong C, Lu S, Hai Y, Zang L. Biomechanical effect of interspinous dynamic stabilization adjacent to single-level fusion on range of motion of the transition segment and the adjacent segment. *Clin Biomech (Bristol, Avon)*. 2015;30(4):355-359. doi:10.1016/j.clinbiomech.2015.02.012

157. Dahl MC, Ellingson AM, Mehta HP, Huelman JH, Nuckley DJ. The biomechanics of a multilevel lumbar spine hybrid using nucleus replacement in conjunction with fusion. *Spine J*. 2013(13);2:175-183. doi:10.1016/j.spinee.2012.11.045

158. Hartmann F, Nusselt T, Maier G, Rommens PM, Gercek E. Biomechanical testing of different posterior fusion devices on lumbar spinal range of motion. *Clin Biomech*. 2019;62:121-126. doi:10.1016/j.clinbiomech.2019.01.012

159. Ivicsics MF, Bishop NE, Püschel K, Morlock MM, Huber G. Increase in facet joint loading after nucleotomy in the human lumbar spine. *J Biomech*. 2014(47);7:1712-1717. doi:10.1016/j.jbiomech.2014.02.021